
NANOSCALE MAGNETIC RESONANCE SPECTROSCOPY
USING T_1 RELAXOMETRY WITH NV CENTERS IN
DIAMOND

MASTER THESIS BY
Simon Philipp

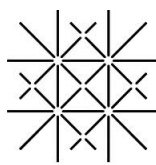
SUPERVISED BY
Prof. Dr. Patrick Maletinsky

DEPARTMENT OF PHYSICS
KLINGELBERGSTRASSE 82
CH-4056 BASEL

AUGUST 24, 2017

Abstract

The coherence time of NV centers in diamond nanostructures is drastically reduced compared to bulk values. The reason for this is part of on going research. Investigation of this effect can be achieved measuring magnetic resonance spectra using T_1 relaxometry of NV centers in diamond. To this end, a confocal microscope including a permanent magnet on a closed loop positioning stage was built. Its functionality was proved by measuring electron paramagnetic resonances at ≈ 500 G in a $\langle 113 \rangle$ oriented diamond with preferentially oriented NV centers.



UNI
BASEL

Contents

1	Introduction	1
2	Theory	4
2.1	NV center	4
2.1.1	General introduction	4
2.1.2	Magnetic field dependent photoluminescence	5
2.2	Magnetic resonance detected by T_1 relaxometry	10
2.2.1	Relaxation	11
2.2.2	Dephasing	13
2.2.3	Magnetic Resonance detection	17
3	Experiment	21
3.1	Accousto-optic modulator Setup	22
3.2	Excitation and Detection	22
3.3	Magnetic field	24
3.4	Microwave	24
3.5	Sample positioning	25
4	Results and discussion	26
4.1	Sample	26
4.2	Magnetic field control	30
4.3	Magnetic resonance	32
4.4	Estimation of P1 density	37
5	Summary and outlook	39
6	Acknowledgments	40
7	APPENDIX	41
7.1	A: Description of LaserPower GUI	41
7.2	B: Description of MagnetPositioner GUI	43
7.3	C: Description of Spectrum GUI	45
7.4	D: List of figures	46

1 Introduction

The Nitrogen-Vacancy (NV) center in diamond has emerged as one of the most prominent defects in the diamond lattice over the last years due to its applications in quantum sensing [1, 2], quantum information processing [3] and diamond based photonics [4]. Recent developments include for example the quantitative detection of vortex states in superconductors [5], detection of magnetic resonances [6, 7] or the excitation of surface plasmon polaritons [8]. It stands out due to its long room temperature T_2 coherence time of up to two milliseconds [9], which is vital for all kinds of quantum technology. In magnetic sensing applications, for example, this enables sensitivities in the regime of a few nT/ $\sqrt{\text{Hz}}$, allowing for the detection of weak magnetic phenomena at the nano scale [10]. Being used as a sensor in a scanning probe, its atomic size at the same time facilitates high spacial resolution. Optical read out of the spin state, as well as manipulation of the state via a microwave driving field, makes it a robust solid state quantum system for sensing purposes.

A drawback to using the NV in a scanning probe system is that the coherence time of the NV center is reduced, if it is located near the diamond surface [11, 12, 13]. This effect is most likely due to spins [14] and charge distributions [15] on the surface of the diamond. However, shallow implanted NVs are vital for the detection of signals external to the diamond. As these signals drop off very fast, it is important to get as close to the sample as possible. In scanning probe magnetometry, the spacial resolution of the image depends on the distance to the sample. To improve the spacial resolution, nano structures such as pillars are fabricated containing near surface NVs to minimize the distance to the sample. In addition to the surface related shortening of T_2 , the NV loses coherence if located in a nano structure.

The reasons for this are still ambiguous and part of current research. A possible explanation could be the occurrence of additional spins and charges resulting from the fabrication process. Fabrication of nanostructures in diamond requires etching procedures including plasmas and reactive ion beams [10]. Such treatments probably produce unpaired electrons from dangling bonds on the diamond surface that might couple to the NV spin. Free radicals from the etching procedure could diffuse into the nanostructure, contributing to the spin bath that affects the T_2 time of the NV center.

The electronic structure of atoms or molecules can be probed using electron spin resonance (ESR) spectroscopy. Measuring the absorption of an oscillating magnetic field in the presence of a static magnetic field, the magnetic dipole transitions (Zeemann transitions) can be directly observed. Knowing the gyromagnetic ratios of the constituents in the sample allows for the extraction of a spectrum of the contributing electronic spins. An

analog procedure for the chemical structure is called nuclear magnetic resonance (NMR) spectroscopy. In contrast to ESR, however, the field acting on a nucleus consists of two parts: the applied static external field and a local oscillating field generated by the adjacent nuclear spins, due to their Larmor precession [16]. The local field screens the nucleus from the external field, which causes the resonance frequency of the transition to depend on the local field. Measuring the absorption of an oscillating field (e.g. a microwave field) therefore contains information about the magnetic environment of the nucleus and hence the chemical structure of, for example, a molecule [17].

Application of these methods, however, is restricted to high magnetic fields and large samples, due to the weak signal strength of the investigated spins. To measure signals arising from the environment of the NV center, it is vital to bring the NMR technique to the nanoscale. This can be achieved by using the NV itself as a sensor, thereby providing all optical read out of the signal. There are in general several ways to measure magnetic resonances, based on the measurement of either the relaxation time, T_1 , or the coherence time T_2 of the NV spin. T_2 based schemes employ complex microwave pulsing sequences, either to drive the target spins in the case of detecting electron spins through a double electron-electron resonance (DEER) sequence, [18] or, in the case of detecting nuclear spins, to employ dynamical decoupling sequences [19] as a frequency filter to probe the magnetic noise generated by nuclear spins.

Even though it is possible to extract information about the environment in this way, T_2 based methods have to struggle with several issues. For example, application of pulsing sequences can be challenging from an experimental point of view: Generation of the pulses and delivery to the sample can affect both pulse length, intensity and sequential arrangement, directly limiting the sensitivity of the measurement. A more fundamental problem in employing T_2 methods to probe the cause of the reduced coherence time is that the interrogation time for these measurements is limited by T_2 , whose shortening is the central problem. This limits the sensitivity of these methods [20, 14].

Detection of magnetic resonances via T_1 based measurement schemes are inherently immune to such complications. Not only is the T_1 measurement scheme able to be implemented without microwave pulsing, which makes it an easily controllable, robust method, but T_1 can also be up to three orders of magnitude longer for near surface NV centers [20, 14]. T_1 based magnetic resonance detection has been proven recently for a single NV spin by Hall *et. al.* [21]. The T_1 relaxation time of the NV spin is measured as a function of the external magnetic field. Magnetic resonance spectra can be obtained by measuring the reduction in T_1 , resulting from the dipole-dipole mediated energy exchange if the probe spin is in resonance with environmental spins. Using the NV center as a probe system for this measurement method makes it a unique, broadband sensor for both ESR

and NMR at the nanoscale.

This thesis presents the implementation of the equipment to detect magnetic resonances in nanostructures into a versatile room temperature confocal microscope and proves its functionality by measuring electron paramagnetic resonance spectra in a field regime around 500 G. After an introduction to the NV center and its magnetic field dependent photodynamics, the theoretical principle of T_1 based magnetic resonance spectroscopy is explained. The description of the setup is followed by the discussion of the experimental results.

2 Theory

2.1 NV center

2.1.1 General introduction

The NV defect in the diamond lattice consists of a substitutional nitrogen atom sitting at a carbon lattice site, with an empty site (vacancy) next to it. It naturally occurs in two charge states: the negatively charged one with one free electron (NV^-) and the neutral one (NV^0). Conversion to a positive charge state, the NV^+ is possible, however it requires the removal of another electron by manipulating the electric environment of the center for example via Schottky contacts [22, 23]. The NV^- state exhibits a unique electronic spin structure, allowing for easy control and all optical read out of the spin state due to its spin dependent photoluminescence. This renders it extremely useful for applications for example in magnetometry. The thesis will always refer to the NV^- as NV center.

The NVs energy ground and excited state consist of a spin triplet with a zero field splitting of $D_{gs} = 2.87$ GHz between the $m_s = 0$ and the degenerate $m_s = \pm 1$ states in the ground state and (at room temperature) $D_{es} = 1.42$ GHz in the excited state, respectively [24]. The magnetic quantum number m_s describes the spin projection along the quantization axis of the NV, which is at zero field given by the connection between the nitrogen atom and the lattice vacancy. The spin states that correspond to a certain magnetic quantum number m_s will in the following be denoted in the bra-ket notation, e.g. the states with $m_s = 0$ and $m_s = \pm 1$ are denoted as $|0\rangle$ and $|\pm 1\rangle$, respectively. Non-resonant excitation can be achieved via a green laser at a wavelength of 532 nm. The excited state population can in principle decay via two paths: Either directly, emitting a photon or indirectly via an intermediate singlet level, without emitting a photon. Exciting the electron out of one of the $|\pm 1\rangle$ ground state levels yields a higher probability for a decay without emitting a photon via an intermediate singlet level, while excitation out of the $|0\rangle$ state has a high probability for decaying directly (See Fig.(1)). Hence, the spin states with non-zero quantum number appear up to about 30% darker, which allows for optical read-out of the spin state as for example in electron-spin resonance experiments [26].

Applying a magnetic field along the quantization axis of the system splits the $|\pm 1\rangle$ states due to the Zeemann effect by an amount of $\Delta\omega = 2\gamma_{NV}B_{\parallel}$, where $\gamma_{NV} = 2.875$ MHz/G is the electron gyromagnetic ratio [28]. Knowing the transition frequency, the $|\pm 1\rangle$ states can be coherently populated by microwave radiation. Further details to the NV center can be found, for example in [28] or [29].

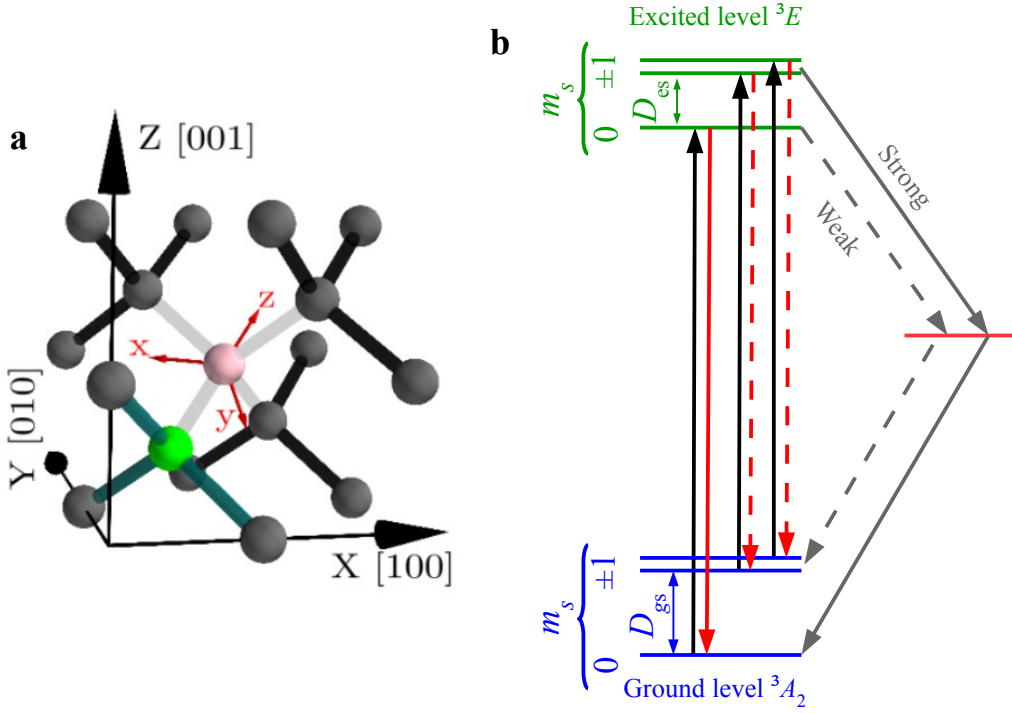


Figure 1: **a** Schematic of the NV center in diamond. A nitrogen atom (green) is located next to a lattice vacancy (pink). The coordinate system indicates the quantization axis along z . **b** Level diagram of the NV center. Spin conserving transitions can be driven via a green laser (black arrows). The $m_s = 0$ states have a high probability for a direct decay via photon emission (red arrow). The $m_s = \pm 1$ states have a high probability for a non-photonic decay via an intermediate singlet level (gray arrows). *Source of a:* [27]

2.1.2 Magnetic field dependent photoluminescence

The Hamiltonian that fully describes the NV center includes interactions with adjacent spins and charges, electric, magnetic and strain fields as well as the hyperfine coupling to the nitrogen atom [30]. At room temperature, however, it has been shown that the photonic response for a given spin state of the NV center mainly depends on the magnetic field and is largely independent of strain or electric fields [31]. As the dependence of the photonic response on magnetic field becomes important in the magnetic field regime required for the carried out experiments, this chapter gives a description of the photoluminescence behavior of NV subject to such fields.

To describe the magnetic field dependent photodynamics of the NV, it is useful to neglect the terms that play a minor role for this problem, such as the hyperfine and strain coupling term, as well as the terms for the electric field. The magnetic field dependence of the NV center's ground state can therefore be described by the following reduced Hamiltonian [32]

$$\mathcal{H}_{gs} = hD_{gs}S_z^2 + g\mu_B\mathbf{B} \cdot \mathbf{S} = \mathcal{H}_{gs}^z + \mathcal{H}_{gs}^\perp \quad (1)$$

where $\mathcal{H}_{gs}^z = hD_{gs}S_z^2 + g\mu_B B_z S_z$ and $\mathcal{H}_{gs}^\perp = g\mu_B(B_x S_x + B_y S_y)$, with h being Planck's constant, μ_B the Bohr magneton and $g \approx 2$ the electron g -factor. The Hamiltonian describing the excited state is simply given by changing the value for D_{gs} to the one of D_{es} in equation (1). Writing this Hamiltonian in matrix form in the basis $\{|-1\rangle, |0\rangle, |+1\rangle\}$ yields

$$\mathcal{H}_{gs} = \begin{pmatrix} D_{gs} + \frac{B_z g_e \mu_B}{h} & \frac{(B_x - iB_y) g_e \mu_B}{\sqrt{2}h} & 0 \\ \frac{(B_x + iB_y) g_e \mu_B}{\sqrt{2}h} & 0 & \frac{(B_x - iB_y) g_e \mu_B}{\sqrt{2}h} \\ 0 & \frac{(B_x + iB_y) g_e \mu_B}{\sqrt{2}h} & D_{gs} - \frac{B_z g_e \mu_B}{h} \end{pmatrix} \quad (2)$$

The on diagonal terms only depend on B_z and describe the Zeemann splitting between the $|0\rangle$ and the $|\pm 1\rangle$ states, whereas the off diagonal terms depend on the transverse magnetic field components and induce a mixing of the $|0\rangle$ and $|\pm 1\rangle$ states. The elements in the upper right and lower left corners of the matrix would be responsible for the coupling of the $|+1\rangle$ and $|-1\rangle$ states, which is achieved for example by a strain field [33] or an electric field [15]. As the strain and electric field dependence has been neglected in the Hamiltonian, these elements are zero.

The transverse fields are zero if the magnetic field is perfectly aligned with the NV axis and the corresponding Eigenenergies are $E_{+1} = D_{gs} + \frac{B_z g_e \mu_B}{h}$, $E_{-1} = D_{gs} - \frac{B_z g_e \mu_B}{h}$ and $E_0 = 0$, for spin $|+1\rangle$, $|-1\rangle$ and $|+0\rangle$, respectively. As already mentioned above, the Hamiltonian of the excited state is given by replacing D_{gs} by D_{es} and consequently, the excited state shows an equivalent structure as the ground state with the same quantization axis, differing only in the value of the zero field splitting.

The dynamics of the population of the states while subject to laser illumination at zero field can be modeled by introducing transition rates $k_{ij}^0 : i, j \in \{1, 7\}$ for a seven level model, including the six states from ground and excited state and one additional intermediate, metastable level [32]. Actually, the structure of the metastable state has not been understood very well for a long time and is still studied extensively by many groups, both in experiment and theory [34, 35]. Results of infrared emission experiments identified two singlet levels, 1E and 1A rather than only one [36].

State	m_s	Label
Ground	0	$ 1^0\rangle$
	-1	$ 2^0\rangle$
	+1	$ 3^0\rangle$
Excited	0	$ 4^0\rangle$
	-1	$ 5^0\rangle$
	+1	$ 6^0\rangle$
Intermediate	-	$ 7^0\rangle$

Table 1: Labeling of NV states

The lifetime of the upper of the two singlet level is supposed to be shorter than 30 ns, which is a factor of 10 shorter than the overall life time of ≈ 300 ns of the intermediate state [36]. Therefore, the singlet manifold can be treated as one level without loss of generality in our description. To introduce the rate model, it is useful to label the seven states as can be seen in Table (2.1.2).

The superscript zero labels the states in the zero field regime. Applying an external magnetic field which is not perfectly aligned with the NV axis increases the off-diagonal terms in equation (2) and the states mix as follows [32]:

$$|i\rangle = \sum_{j=1}^7 \alpha_{ij} |j^0\rangle \quad (3)$$

where α_{ij} is a mixing parameter. The matrix α is a seven times seven matrix which can be computed numerically by calculating the values for B_x , B_y and $D_{gs/es} \pm \frac{B_z g_e \mu_B}{h}$ from the angle by which the field is misaligned from the NV symmetry axis. Using the Matrix representation of the Hamiltonian from equation (2), α is given as follows:

$$\alpha = \begin{pmatrix} \mathcal{H}_{gs} & 0 \\ & \mathcal{H}_{es} \\ 0 & 1 \end{pmatrix} \quad (4)$$

As the interaction of the intermediate state with the external magnetic field is assumed to be too weak to induce any state mixing, the according matrix element is equal to one and therefore $|7\rangle = |7^0\rangle$.

In the zero field regime, transitions k_{ij}^0 between states $|i^0\rangle$ and $|j^0\rangle$ in ground and excited level, respectively, can be considered as fully spin conserving, while the radiative relaxation from the excited state to the ground state is spin independent ($k_{41}^0 = k_{52}^0 = k_{63}^0 = k_r^0$) [32]. The transition rates from the excited state to the intermediate level depend on m_s , such that $k_{57}^0 = k_{67}^0$. While $k_{47}^0 \ll (k_{57}^0, k_{67}^0)$, the situation is opposing

for the transitions from the intermediate state to the ground state, such that $k_{72}^0 = k_{73}^0$ but $k_{71}^0 \gg (k_{72}^0, k_{73}^0)$. This causes the spin dependent fluorescence mentioned in the general introduction. The situation changes, however, when the external magnetic field is misaligned with the NV axis and the transverse fields become large compared to the parallel component. The quantization axis is then rather given by the external magnetic field than by the NV symmetry axis and m_s is no longer a good quantum number. The Eigenstates of the Hamiltonian are then given by equation (3) and the spin conservation of the transition breaks down. Hence, the transition rates change as well, given by the following relation [32]:

$$k_{ij} = \sum_{p=1}^7 \sum_{q=1}^7 |\alpha_{ip}|^2 |\alpha_{jq}|^2 k_{pq}^0 \quad (5)$$

which is a statistical averaging, using the values from Eq. (4) as weights. This implies that the relations between the ground and excited state and the intermediate level are no longer valid and all transitions have to be taken into account separately. This, in turn, enhances the probability for a non-radiative decay via the singlet level and the overall fluorescence drops.

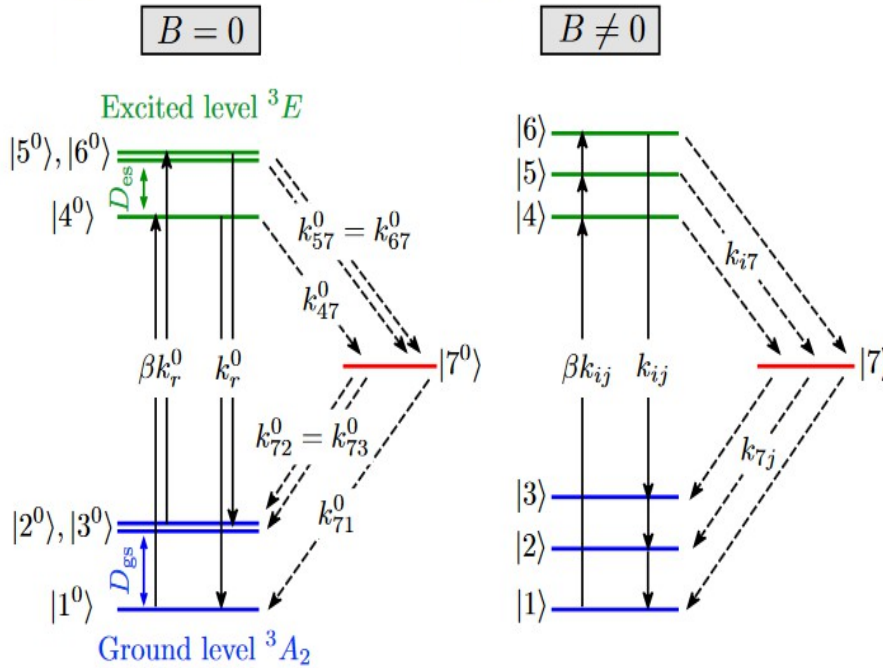


Figure 2: Comparison of the behavior of the transition rates with and without magnetic field. As soon as the external field is applied to the NV, the system is described by new eigenstates and modified transitions. Source: [32]

In the low transverse field regime, the photoluminescence is relatively robust against a misalignment of the external magnetic field, as spin conserving transitions are still efficient even if the transverse components are non zero. This is due to the, compared to D_{gs} , relatively small Zeemann splitting of the states with non-zero magnetic quantum number and hence the well defined separation between the $|0\rangle$ and $|\pm 1\rangle$ states, which makes the coupling very inefficient. As the system approaches parallel fields in the range of $B_z \approx 500$ G, the large Zeemann splitting in the excited state causes the $|0\rangle$ and $|-1\rangle$ states to cross. At this point, the NV is much more sensitive to small transverse fields, as it becomes much more efficient to couple the states. Hence, most of the fluorescence is quenched if the external field is slightly misaligned. The same effect happens at $B_z \approx 1024$ G, due to the equivalent state crossing in the ground state (GSLAC).

The behavior of the the PL as a function of the misalignment angle was studied in [37]. As can be seen from Fig.(3), even small misalignment angles drastically quench the fluorescence of the NV.

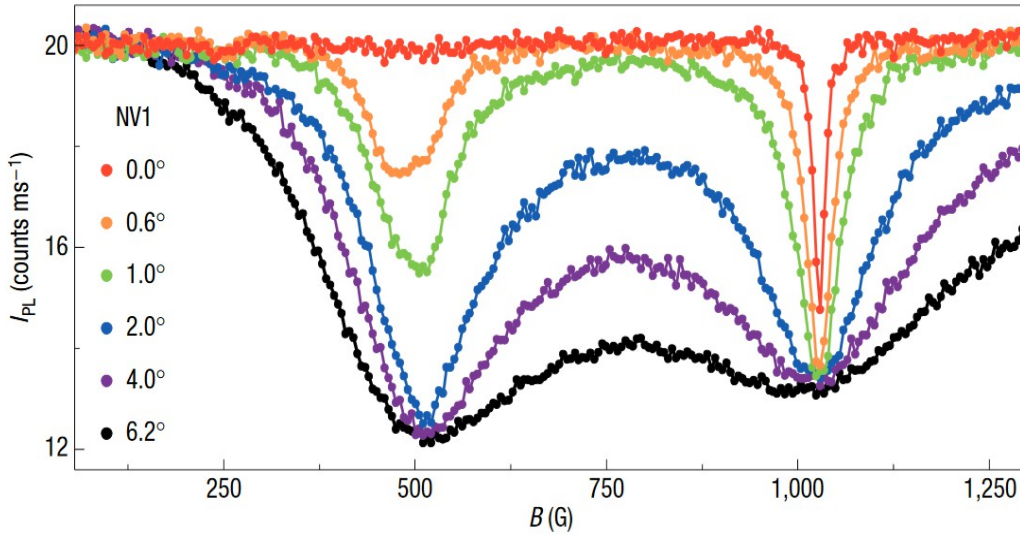


Figure 3: Fluorescence intensity as a function of the external magnetic field for different misalignment angles of the NV to the external magnetic field. Even for small angles, the fluorescence is strongly quenched. *Source:*[37]

2.2 Magnetic resonance detected by T_1 relaxometry

Magnetic resonance spectroscopy has become one of the most prominent methods in life science, medicine, solid state physics and materials science, as it provides a method to gain insights into the structure of solids, as well as organic or living specimens. The electronic, as well as the chemical structure of atoms or molecules can be probed using electron spin resonance (ESR) and nuclear magnetic resonance (NMR) spectroscopy. Both methods are in general based on the absorption of an oscillating magnetic fields in the presence of a static magnetic field. For medical applications, NMR even allows for three dimensional reconstruction of complex structures like brains. Dynamical processes such as diffusion can be measured using the combination of several external fields, as for example in field gradient NMR [38].

Due to the weak signals, these methods are limited to large samples and high fields. To apply the methods to our experiments, we need means to bring NMR to the nanoscale. Given its atomic size, this can be achieved by using the NV spin itself to probe its environment. To obtain the spectra, the NV spin is first initialized in the $|0\rangle$ state. Due to its interaction with the environment, the spin will not remain in its initial state. Rather than that, it will evolve into different state which consists of a mixture between $|0\rangle$ and $|\pm 1\rangle$.

In general, there are two kinds of processes that cause the probe spin to evolve away from its initial state towards thermal equilibrium. The first one is based on the exchange of energy between probe and target and is referred to as relaxation. Since the NV spin is oriented parallel to the magnetic field in this case, it is sensitive to components of the environmental noise spectral density that are in resonance with the $|0\rangle \rightarrow |-1\rangle$ or the $|0\rangle \rightarrow |1\rangle$ transition. This transition happens on a given, system dependent characteristic time scale T_1 . Unless the system is brought into resonance with an environmental component, the T_1 decay is mainly induced by phonons. The second one describes the loss of quantum information and is referred to as dephasing. In contrast to relaxation, the spin is brought in a state perpendicular to the magnetic field. Now, this process is sensitive to magnetic fields at any frequencies, effectively causing a rotation of the spin at the Larmor frequency around the effective magnetic field. The characteristic time scales for this kind of process are called T_2 and T_2^* , respectively. The discussion about the difference between the two shall be left for section 2.2.2. Because of its particular robustness and simplicity, magnetic resonances in our experiments are read out via the change in relaxation rate $\Gamma_1 = 1/T_1$.

In the following, the relaxation and dephasing processes, as well as their application in magnetic resonance detection shall be discussed in some detail. In general, this chapter follows reference [39]

2.2.1 Relaxation

Spins in a solid state system are inherently subject to interactions with the environment. In particular, the system may exchange energy with the spin which causes the spin to relax from an initial, non-equilibrium state towards a state of thermal equilibrium. For the NV center, this means an equal superposition between all three ground state spin levels. The percentage of population of each state in equilibrium will depend on the relative transition rates between the states [39].

The relaxation of the NV spin can be measured by applying a simple measurement sequence, which shall be called T_1 sequence (see Fig.(4)). Usually, the center is initialized in the $|0\rangle$ state via laser illumination. After a free evolution time τ , where the NV spin only interacts with the environment, the population of the $|0\rangle$ state is read out via another laser pulse. At room temperature, the relaxation process is dominated by two-phonon Orbach processes [20, 40]. Other contributions such as magnetic fluctuations at random frequencies resulting from the (temperature independent) dipole-dipole interaction of the NV spin with its environment play a minor role at high temperatures. Dipole-dipole coupling becomes dominant at low temperatures, since the phononic interaction is highly suppressed. As it is of didactic value for the next chapter, the response of the NV to a fluctuating field shall be described below.

Due to the large zero field splitting, off resonant relaxation is driven via Orbach-type processes. Rather than driving transitions between two quantum states directly by absorption or emission of a single phonon, the Orbach process includes two phonons, using a third, intermediate virtual state. After absorbing the first phonon, the intermediate state is populated. Emitting a second phonon of a different wavelength, the population is transferred to the third level [41]. Since this happens simultaneously between all three NV spin states, the two-phonon based relaxation can be approximated by the assumption of direct, constant¹ two-way transition rates k_{ph} between all states (See Fig.(5)). As soon as the NV spin is initialized in one of the energy levels, these rates induce it to relax towards equilibrium. This description is the basis for the detection of magnetic resonances, and will be extended in section 2.2.3.

To understand the response of the NV center to random fluctuations, it is helpful to imagine the influence of a driving field at a single frequency in resonance with the transition between, for example $|0\rangle$ and $|-1\rangle$. The NV spin is then rotated between the two states, resulting in an oscillation of the spin population. This is widely known as Rabi oscillations [42]. The population of the $|0\rangle$ state is then $\mathcal{P}_{|0\rangle}(t) \propto \sin^2\left(\frac{\Omega_R t}{2}\right)$, where Ω_R is the Rabi frequency. Note that, since $\mathcal{P}_{|0\rangle} + \mathcal{P}_{|-1\rangle} = 1$, the population for the $|-1\rangle$ state follows the same dependence, being phase shifted such that $\mathcal{P}_{|-1\rangle} = 0$ for $\mathcal{P}_{|0\rangle} = 1$

¹Note that despite the rates are assumed to be constant, they might still differ in value.

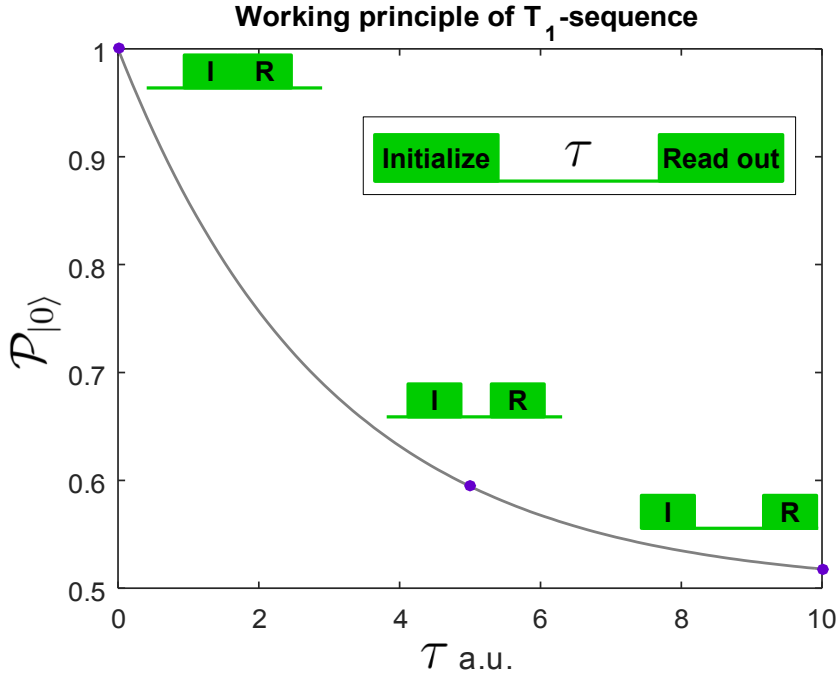


Figure 4: Working principle of the T_1 -sequence (inset). After initializing the NV in the $|0\rangle$ state, the system is left to evolve freely for a time τ . Subsequently, the population $\mathcal{P}_{|0\rangle}$ is read out via a second laser pulse. Repeating the experiment for different values of τ exhibits an exponential decay of the population towards an equilibrium state. Neglecting the contribution to the $|-1\rangle$ state, the population will be equally distributed over the $|0\rangle$ and $|-1\rangle$ states, resulting in an asymptote at $\mathcal{P}_{|0\rangle} = 0.5$.

and vice versa. This can be used to flip the spin by applying the driving field for half a period. Due to this, such an application shall be referred to as a π pulse. This will be of particular importance in the following section.

The resonant part of the random fluctuating field that drives the Rabi oscillations during the interaction time τ can be assumed as a weak field, which is constantly on. Looking at a short time interval, the response to the field can be described as follows: Both dephasing and Rabi oscillations happen simultaneously. Due to their relative strength, the dephasing process happens on a much faster time scale, such that the phase information of the driven Rabi oscillation is lost long before the end of the interval. This prevents the system from performing actual, clearly defined oscillations. Rather than that, only the projection of the spin state to the quantization axis can be measured, resulting in a population distribution among the participating quantum states. Due to the loss of the phase coherence, the process remains static as soon as it reaches $\mathcal{P}_{|0\rangle} = 0.5$. The measured dynamics thus exhibit an exponential decay from the initial state to equilibrium, as it was the case for the phononic interaction.

In a fluctuating field with many different frequencies, every frequency couples dif-

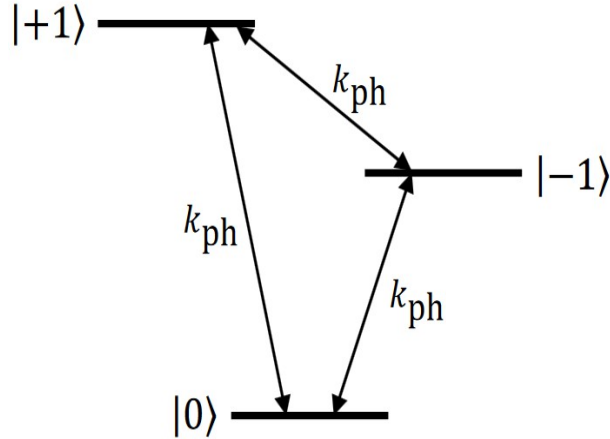


Figure 5: Phonon induced transition rates. Phononic interactions of the NV with the diamond lattice causes relaxation of the NV spin. This can be described with constant transition rates between all three ground state levels. *Source:* [20]

ferently to the NV, depending on their relative strength and detuning from the current transition frequency between the states [39]. Of course, the contribution which is not detuned from the transition has the strongest coupling and therefore the largest influence on the evolution of the spin state. As can be seen from this, the T_1 measurement protocol acts as a frequency filter for the spectral component matching the energy separation of the spin states, which depends on the external magnetic field. The filter function is given by the Lorentzian describing the transition between the states as a function of the detuning. The T_1 measurement can thereby be thought of as an ‘inverse’ electron spin resonance experiment. In ESR, an oscillating field is applied to the NV to get information about the static external field while in the Ramsey experiment a static field is applied to get information about the dynamic components acting on the NV center.

The possibility to scan the filter function across the spectral density of the environment by tuning the external magnetic field will be of fundamental importance for the detection of magnetic resonances, as shall be discussed in section 2.2.3.

2.2.2 Dephasing

As described in the section above, the T_1 -sequence is sensitive to random fluctuations in the environment. However, it lacks the possibility to measure constantly oscillating fields, originating for example from the collective Larmor precession of adjacent nuclear spins. Many of such contributions appear at frequencies in the sub GHz regime, which can not be measured with the T_1 -sequence due to the large zero field splitting in the NV ground state [39]. Getting access to these contributions therefore requires a more complex protocol, that brings the NV spin into a sensitive state. This possibility is provided by

the Free Induction Decay (FID) protocol, or Ramsey sequence, which is characterized by a characteristic decay time T_2^* . For this kind of protocol, the NV spin is brought in a superposition between $|0\rangle$ and $|-1\rangle$ before the resulting state is again left to evolve under the influence of the environment. In contrast to the T_1 -sequence, the difference in population is achieved by a phase shift between the $|0\rangle$ and $|-1\rangle$ state which arises during the evolution time.

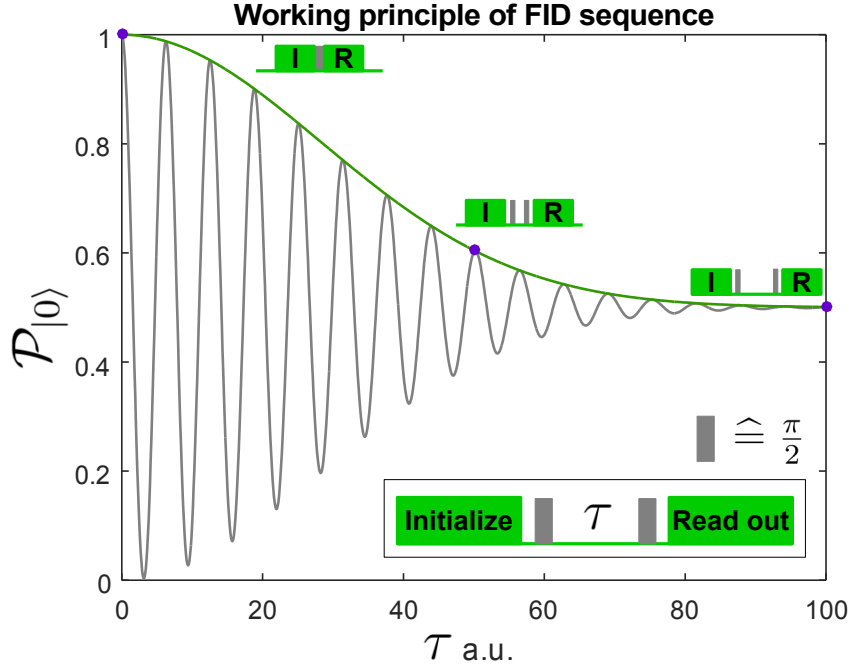


Figure 6: Working principle of Ramsey sequence (inset). As for the T_1 -sequence, the spin is initialized and read out via a green laser pulse. Before the system is left to evolve, a $\frac{\pi}{2}$ pulse brings it into a superposition between $|0\rangle$ and $|-1\rangle$ to make it sensitive to transverse components of the environment. The second $\frac{\pi}{2}$ pulse transforms the resulting phase shift in a difference in population. The envelope (green line) depends exponentially on $\frac{1}{T_2^*}$

Bringing the NV spin in a superposition state can be achieved by populating both spin states equally within the coherence time of the spin state. As can be seen in section 2.2.1, application of a π pulse inverts the populations of the spin states. Consequently, the application of a pulse with the same frequency but only half the duration (a quarter of the Rabi period) equally spreads the population over the two states. We will refer to this as a $\frac{\pi}{2}$ pulse. The spin is now rotated to a state perpendicular to the quantization axis, which makes it sensitive to the magnetic contributions from the environment oscillating at low frequency, $b(t)$. It is easy to see that only the $|-1\rangle$ state is affected by $b(t)$ due to the non-zero magnetic quantum number. As a result, the population $\mathcal{P}_{|0\rangle}(t)$ is given as

$$\mathcal{P}_{|0\rangle}(t) = \frac{1}{2} + \frac{1}{2}\cos(\phi(t)) \quad (6)$$

which is a composition of the constant contribution of the $|0\rangle$ state and the contribution of the $|-1\rangle$ state, which is phase shifted with respect to the $|0\rangle$ state by a phase $\phi(t) = \int_0^t b(t')dt'$. Due to the cosine dependence, $\mathcal{P}_{|0\rangle}(t)$ can reach values between zero and one. However, the description still lacks any ‘damping’ term that induces the decay to equilibrium. The term can be included by taking into account the variation of $\phi(t)$, which is normally distributed for a given instant in time. Inserting the distribution with mean value $\langle\phi\rangle$ and variance $\langle\phi^2\rangle$ into equation (7) yields

$$\begin{aligned}\langle\mathcal{P}_{|0\rangle}\rangle &= \frac{1}{2} + \frac{1}{2} \frac{1}{\sqrt{2\pi\langle\phi^2\rangle}} \int_{-\infty}^{\infty} \exp\left(-\frac{(\langle\phi\rangle - \langle\phi^2\rangle)^2}{2\langle\phi^2\rangle}\right) \cos(\phi)d\phi \\ &= \frac{1}{2} + \frac{1}{2} e^{-\langle\phi^2\rangle/2} \cos(\phi(t)) \\ &= \mathcal{P}_{|0\rangle} e^{-\langle\phi^2\rangle/2}\end{aligned}\tag{7}$$

The oscillations in the population are now modified with a Gaussian envelope. The factor $\langle\phi^2\rangle$ in the exponential is related to the effective field acting on the NV as described above. In turn, the dynamics of the field depends on the spin species from which the field originates [39]. Due to the slow internal dynamics (sub-kHz regime) of a nuclear spin bath (most of which is usually composed of ^{13}C), the envelope is a Gaussian. For an electron spin bath, whose internal dynamics occur on the MHz scale, the envelope appears to be a single exponential decay [39]. In reality, however, usually several spin species contribute to the shape of the envelope and the transition from Gaussian to exponential decay is quite smooth. This behavior can be modeled by writing the averaged population as [43]

$$\langle\mathcal{P}_{|0\rangle}\rangle = \mathcal{P}_{|0\rangle} e^{-\left(\frac{\tau}{T_2^*}\right)^\epsilon}\tag{8}$$

where $\epsilon \in [1, 2]$. The dependence of ϵ on the shape of the envelope is shown in Fig.(7). Since the decay time of the signal is comparatively short, the effective field acting on the NV appears quasi-static. Hence, the FID protocol lacks the description of the dynamics of the spin bath. Investigation of the dynamic properties thus requires a means to extend the decay time. This can be achieved via the application of more complex pulse sequences, as for example the spin-echo or Hahn-echo sequence [44], which employs a π pulse at $\tau/2$ to flip the NV spin, effectively eliminating the static contributions of the environment to the signal. The decay time-scale is now characterized by a characteristic time constant T_2 , which, by definition, is equal or longer than T_2^* [15]. As it is not of particular importance for the experiments in this case, a full description of this sequences would be out of the scope of this thesis. For the sake of completeness, it shall be noted that the Hahn-echo sequence is only the simplest of a large variety of pulse sequences, all

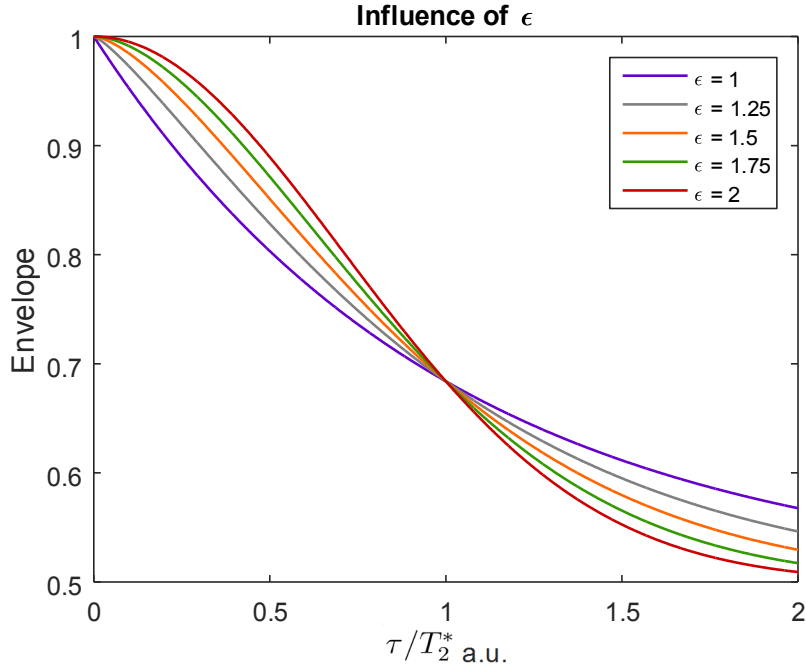


Figure 7: Influence of ϵ on the envelope of the FID signal. $\epsilon = 1$ corresponds to an electron spin bath and results in an exponential decay. $\epsilon = 2$ describes a nuclear spin bath and is of Gaussian shape. The shapes of the envelope transform smoothly into each other.

having in common that the number and arrangement of the pulses act as a filter for the investigated environmental noise contribution. Shifting the central frequency of the filter away to higher values, the NV can effectively be decoupled from the bath dynamics, which drastically enhances T_2 [45, 44]. This is of particular importance for applications in, for example, magnetometry, where the sensitivity of the sensor depends on T_2 , as well as quantum information processing, as it defines the time limit for coherent operations to be applied to the NV spin.

Even though magnetic resonances can be detected both via relaxation and dephasing or decoherence experiments, there are several drawbacks using T_2^* or T_2 based protocols. As explained above, these protocols not only require the possibility to manipulate the spin via microwave radiation but also the use of complex pulse sequences, which are inherently susceptible to pulsing errors. Using relaxation methods, however, provides all optical readout without the need of any driving fields during the evolution time. In addition, the readout time in dephasing and decoherence spectroscopy is limited by T_2 of the NV, which is, in comparison to bulk NVs, drastically reduced in close proximity to the surface [46], limiting the number of target spins to be detected [20]. Using T_1 relaxometry, the limit can be extended to the T_1 time of the center, which is much longer for near surface NVs.

The principle of magnetic resonance and its detection by T_1 relaxometry shall be described in the following section.

2.2.3 Magnetic Resonance detection

The fundamental principle of magnetic resonance is the dipolar coupling of the (environmental) target spins to the probe spin. The interaction energy of two magnetic dipoles can be derived in analogy to the multipole expansion of the energy of a charge distribution in an external field, as it is done in electro-statics. It is described by the dipole term of the expansion $W_{\text{dipole}} = \mathbf{p} \cdot \mathbf{B}$ (cf. [47], eq. 4.24 for electrostatic analog), where \mathbf{p} is the dipole moment and \mathbf{B} is the field which it interacts with. Assuming $\mathbf{p} = \mathbf{m}_{\text{p}}$ to be the magnetic moment of the probe spin (NV spin in this case) and $\mathbf{B}(\mathbf{r}) = \frac{\mu_0}{4\pi} \left[\frac{3\hat{\mathbf{r}}(\hat{\mathbf{r}} \cdot \mathbf{m}_{\text{t}}) - \mathbf{m}_{\text{t}}}{|\mathbf{r}|^3} + \frac{8\pi}{3} \mathbf{m}_{\text{t}} \delta(\mathbf{r}) \right]$ the field of the target spin, where \mathbf{r} is the probe-target distance, \mathbf{m}_{t} is the magnetic moment of the target spin, $\hat{\mathbf{r}}$ a unit vector along the connection of the two spins and $\delta(\mathbf{r})$ the delta function, the interaction energy of the two dipoles reads

$$\begin{aligned} W_{\text{p,t}} &= \mathbf{m}_{\text{p}} \cdot \mathbf{B}(\mathbf{r}) \\ &= \mathbf{m}_{\text{p}} \cdot \frac{\mu_0}{4\pi} \left[\frac{3\hat{\mathbf{r}}(\hat{\mathbf{r}} \cdot \mathbf{m}_{\text{t}}) - \mathbf{m}_{\text{t}}}{|\mathbf{r}|^3} + \frac{8\pi}{3} \mathbf{m}_{\text{t}} \delta(\mathbf{r}) \right] \\ &= \frac{\mu_0}{4\pi} \left[\frac{3(\mathbf{m}_{\text{p}} \cdot \hat{\mathbf{r}})(\mathbf{m}_{\text{t}} \cdot \hat{\mathbf{r}}) - \mathbf{m}_{\text{p}} \cdot \mathbf{m}_{\text{t}}}{|\mathbf{r}|^3} \right] \end{aligned} \quad (9)$$

Since probe and target spin never reside at the same place, the term proportional to the delta function drops out. As $W_{\text{p,t}}$ is a scalar value that depends mainly on the probe-target distance, the interaction energy differs for target spins at different distances. Note that expanding the description to an ensemble of targets can be achieved by integrating over a target spin density and an average distance.

Until now, there is no energy exchange between the target spin and the NV, as the transition frequencies between the half integer electron spin states in the environment differs from the one of the integer spin states in the NV ground state. The target transitions can be brought into resonance with the $|0\rangle \rightarrow |-1\rangle$ transition of the NV via the Zeemann effect by applying an external magnetic field [20]. The transition frequency of the target spins can be described as $\omega_{\text{t}}(B) = D_{\text{t}} + \gamma_{\text{t}} B_{\text{ext}}$, where γ_{t} the gyromagnetic ratio of the target spin and D_{t} its intrinsic splitting, which may include all kinds of interactions like zero field splittings, hyper fine interactions etc. From this, a resonance condition can be formulated [20]:

$$|\omega_{\text{NV}}(B_{\text{res}})| = |\omega_{\text{t}}(B_{\text{res}})| \quad (10)$$

With $\omega_{\text{NV}}(B) = D_{gs} + \gamma_{\text{NV}}B_{\text{ext}}$ as described above. Plugging ω_{NV} and ω_t into eq.(10) yields the values for B_{res} :

$$B_{\text{res}}^{\pm} = \left| \frac{D_{\text{NV}} \pm D_t}{\gamma_{\text{NV}} \pm \gamma_t} \right| \quad (11)$$

For electronic spins, the resonant field is around $B_{\text{res}} \sim 512$ G. This corresponds to transition frequencies in the range of $\omega_{\text{NV},t} \sim 1 - 2$ GHz. The values of B_{res}^- are basically identical to the ones of B_{res}^+ , only for an external magnetic field with opposite direction and the $|0\rangle \rightarrow |+1\rangle$ transition. Therefore, only $B_{\text{res}}^+ \equiv B_{\text{res}}$ is taken into account for the electrons. As their gyromagnetic ratio is much smaller than the one for electrons, nuclear spins require fields as high as $B_{\text{res}} \sim 1024$ G. As they lie on both sides of the GSLAC, respectively, both B_{res}^- and B_{res}^+ are of relevance (See Fig.(8)).

As soon as the transition frequencies match, the NV starts to exchange energy due to the coupling described by eq.(9). This induces an additional transition rate k_{res} (See Fig.(8)) between the corresponding states, effectively reducing T_1 . Investigating T_1 as a function of the external magnetic field, therefore reveals a magnetic resonance (MR) spectrum around the resonant field values.

The relaxation rate associated with a given relaxation or dephasing time T_i is given by $\Gamma_i = 1/T_i$. An expression for the relaxation rate at resonance can be achieved using the Hamiltonian [20]

$$\mathcal{H} = \underbrace{hD_{gs}S_z^2 + \gamma_{\text{NV}}B_zS_z}_{\mathcal{H}_{gs}^z} \underbrace{-h\gamma_tB_zI_z}_{\mathcal{H}_t} - \underbrace{\frac{\mu_0\gamma_{\text{NV}}\gamma_t h^2}{4\pi\mathbf{r}^3} \left[\frac{3}{\mathbf{r}^2} (\mathbf{S} \cdot \hat{\mathbf{r}}) (\mathbf{I} \cdot \hat{\mathbf{r}}) - \mathbf{S} \cdot \mathbf{I} \right]}_{\mathcal{H}_{int}} \quad (12)$$

where \mathbf{I} is the spin operator (either electronic or nuclear) of the target system. \mathcal{H}_{int} is the dipole-dipole interaction term and hence the quantum mechanical version of eq.(9), using $\mathbf{m}_p = \mathbf{m}_{\text{NV}} = \gamma_{\text{NV}}\mathbf{S}$ and $\mathbf{m}_p = \gamma_t\mathbf{I}$. Further, \mathcal{H}_{gs}^z is the parallel part of the NV ground state Hamiltonian as introduced in section 2.1.2 and \mathcal{H}_t the target Hamiltonian. The Hamiltonian is a 4×4 matrix whose off diagonal elements are interaction terms arising from \mathcal{H}_{int} . The on-diagonal terms describe the Zeemann splitting of the NV, as well as the target spin states and can therefore be used to derive the equations for the relaxation rates. Note that the on-diagonal terms also include interaction terms in the resonance condition. Assuming a weak dipolar coupling, these terms can be neglected resulting in eq.(11).

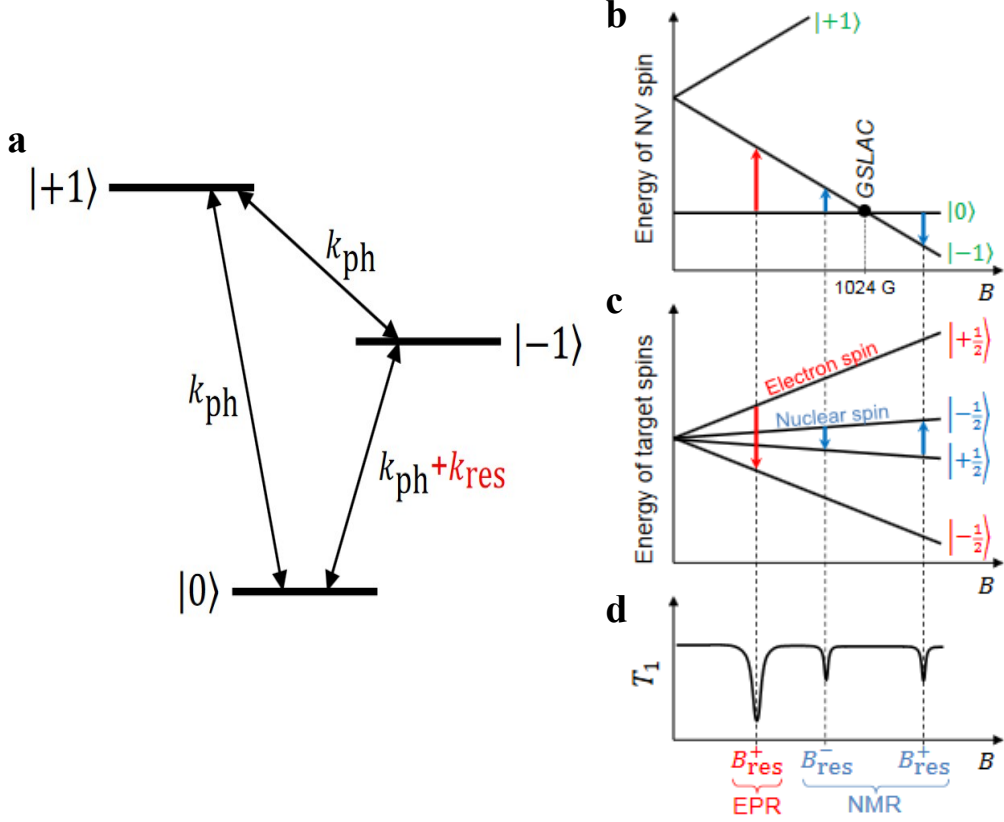


Figure 8: **a** Relaxation rates at resonance. If the $|0\rangle \rightarrow |-1\rangle$ transition in the NV ground state is in resonance with transitions of target spins, a rate k_{res} is induced via the energy exchange between target spin and NV center, effectively reducing T_1 of the system. **b** Zeemann splitting of NV ground state levels. Around $B_{\text{res}} \sim 1024$ G, the $|-1\rangle$ and the $|0\rangle$ states anti-cross (Ground State Level Anti-Crossing). **c** Zeemann splitting of the target spins. Due to the smaller gyromagnetic ratio, the nuclear spin states split more slowly. The narrow transitions are resonant with the NV around the GSLAC. **d** Schematic illustration of T_1 relaxometry. The T_1 time of the NV spin is measured as a function of the external magnetic field. As soon as the NV transition is in resonance with target transitions (red and blue arrows in **b** and **c**), a dip in the spectrum occurs. As described in the text, there are two resonant fields for the nuclear magnetic resonance (NMR) and only one resonant field for the electron paramagnetic resonance (EPR).

Using the density matrix formalism [48], the relaxation rates Γ_1^{EPR} and Γ_1^{NMR} at resonance can be modeled as follows:

$$\Gamma_{1,\text{res}}^{\text{EPR}} = \frac{1}{\Gamma_{2,\text{tot}}^*} \left(\frac{\mu_0 \gamma_{\text{NV}} \gamma_t \hbar}{2\sqrt{2}} \right)^2 \left(\frac{3\sin^2(\theta)}{r^3} \right)^2 \quad (13)$$

$$\Gamma_{1,\text{res}\pm}^{\text{NMR}} = \frac{1}{\Gamma_{2,\text{tot}}^*} \left(\frac{\mu_0 \gamma_{\text{NV}} \gamma_t \hbar}{2\sqrt{2}} \right)^2 \left(\frac{3\sin^2(\theta) - 1 \pm 1}{r^3} \right)^2 \quad (14)$$

where $\Gamma_{2,\text{tot}}^* = \Gamma_{2,\text{NV}}^* + \Gamma_{2,\text{t}}^*$ is the total dephasing rate of both NV and target and θ is the angle of the NV to the external magnetic field.

Without providing a derivation, it shall be noted that $\Gamma_{2,\text{tot}}^*$ is related to the line width of the dips in the ESR/NMR spectrum. A full derivation for this, as well as for Eqs.(13-14) can be found in the supplementary material of [20].

3 Experiment

To access the NV centers, we use a home-built confocal microscope. We use a free beam configuration, where the NV fluorescence is detected directly without coupling it into an optical fiber. Avoiding fibers in the detection path avoids fiber coupling losses and allows for detection of a larger percentage of the NV fluorescence, resulting in a higher photon count rate. Since the signal to noise ratio of all types of measurements where single photons are counted depends inversely on the square root of the counted photons (shot noise), it requires a high number of photons to get a suitable result. Having large photon count rates therefore reduces the integration time for a given experiment. The setup, as sketched in Fig.(9), shall be described in the following.

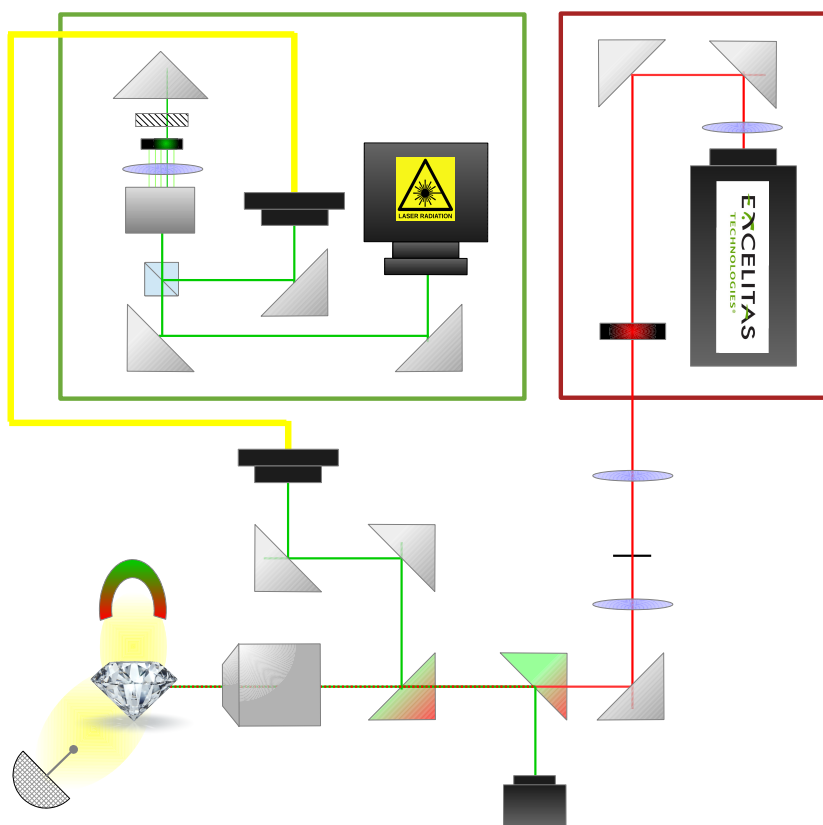


Figure 9: Schematic of the Setup. The accousto-optic modulator (AOM) and the detection setup including the avalanche photodiode (APD) indicated by the green and red surroundings, respectively. The individual parts are described in the text.

3.1 Accousto-optic modulator Setup

Initialization and read out of the NV center’s spin state is achieved via application of green laser light. As many experiments require short laser pulses with a given length and intensity rather than a constant illumination for this process, it is crucial to have good control over switching the laser between the “on” and “off” states with close to nanosecond precision. This can be achieved using an acousto optical modulator (AOM). The AOM itself consists of a photoelastic crystal coupled to a piezoelectric transducer. A sound wave which appears as alternating areas of refractive indices is induced in the crystal by applying an alternating voltage signal to the transducer. The AOM is aligned such that most of the intensity is coupled into the first order maximum of the resulting interference pattern of the beam after passing the crystal. The now bright first maximum is separated by an iris and then reflected back to the AOM. Passing it again guides the modulated beam back to the original beam path. A quarter wave plate in front of the mirror that reflects the first order maximum back to the AOM controls the polarization of the beam and it can be filtered out by a polarizing beam splitter cube. Because of the path through the setup and the switching time of the hardware, there is a delay between the onset of the laser pulse in the control software and the arrival of the actual laser pulse at the sample. This delay time is system dependent and can be measured by monitoring the count rate of the NV for the duration of the laser pulse by sweeping the start point of a short read out pulse from the beginning to the end of the pulse. Taking this delay into account is most notably important in the regime of high polarization rates and in the case of short laser pulses. In this setup, the AOM delay time is ~ 600 ns. In addition to pulsing the laser between on and off states, the intensity of the laser transmitted to the sample can be tuned by increasing the amplitude of the oscillating voltage signal at the piezoelectric transducer. This is achieved by mixing the constant- amplitude sine shaped output from a voltage controlled oscillator (VCO) with a DC voltage which is set by a MATLAB command and provided by the NI hardware. Control of the laser excitation power is useful as it allows to drive NV centers near saturation, which can differ from sample to sample. Furthermore, since the polarization rate of the NV center depends on the laser power, the contrast of continuous ESR measurements can be improved.

3.2 Excitation and Detection

After the double-pass AOM, the beam is guided to the setup via an optical fiber and overlapped with the detection beam path. The light is focused on the sample by a NA 0.9 objective (NIKON, NA = 0.9). Due to the high NA, a large part of the resulting fluorescence is coupled back into the objective and guided back along the beam path of

the excitation laser. It subsequently passes two dichroic mirrors (Semrock RazorEdge, cut on wavelength 514 nm) that filter out the green light from the excitation and enters a telescope subsequently. The telescope itself consists of two plano-convex lenses ($f_1 = 50$ mm, $f_2 = 75$ mm) and has the function to focus the collimated signal beam originating from the focal spot of the green light in the sample to a common focal spot of the two lenses and collimate it again afterward. Placing a pinhole ($R_p = 30$ μm) right into the focal spot of the telescope filters out any access light from the environment of the focal spot in the sample, as its focal spot in the telescope is slightly before the pinhole due to a different entrance angle at the objective. The objective and the pinhole are now confocal, giving the setup its name. Determining the amount of access light passing the telescope, the size of the pinhole directly affects the resolution and the signal to noise ratio of the measured image. [49].

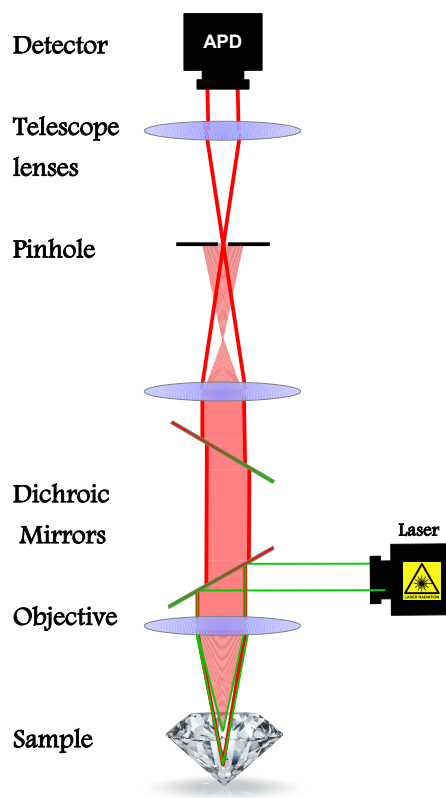


Figure 10: Principle of confocal microscopy. The excitation light is focused on the sample via an objective. Due to the different entrance angle fluorescence that originates from the vicinity of the focal spot is blocked by the pinhole as it is not confocal.

Note that the system could also be used without the pinhole, having a lower resolution. This can be useful in situations where the resolution doesn't play a specific role, as for example while investigating single emitters in photonic structures as pillars, where the origin of the signal is clearly located. Omitting the pinhole dramatically increases the

photon count rate, which enables shorter read-out times for example in magnetometry. Being collimated again by the second lens, the signal beam enters a box in which the detection devices are placed. A high pass filter (Thorlabs...cut on wavelength at....) again filters out any light with wavelength shorter than the NV spectrum (ranging approximately from 550-800 nm). Two mirrors guide the Signal to a lens which focuses the beam onto a chip of an avalanche photo diode (APD). The APD, together with a data-acquisition card (National Instruments 6990), counts the amount of photons arriving with the signal beam.

3.3 Magnetic field

As described in the theory section, the application of external magnetic fields along the quantization axis of the NV center requires precise control of a magnetic field source due to strong photoluminescence (PL) quenching caused by high transverse magnetic field components that appear even at small misalignment angles. Since using a room temperature, table-top vector magnet consisting of three coils doesn't attain high enough fields, the experiment is restricted to using a strong permanent magnet which in turn requires a very precise and stable positioning system. In our setup, we use a combination of three SLC-1730 linear positioners together with the HCU-3D control system by SmarAct. The whole stage has a travel range of $21 \times 21 \times 21 \text{ mm}^3$ and acts in closed-loop mode, which allows for the approach and read-out of absolute positions. It has a sensor resolution of 1 nm with a repeatability better than $\pm 30 \text{ nm}$. The step size of the positioners is 50-1500 nm, in low vibration mode even smaller². The magnet is attached at the end of a metal rod mounted in a right angle at the vertical positioner of the stage. The magnet itself is a permanent neodymium magnet, delivered by www.supermagnete.ch. To control the stage and the magnetic field at the NV location, we wrote a new MATLAB GUI for a proper implementation of the system in our measurement software. The GUI is described in more detail in Appendix 7.2. The code behind the GUI calls the command library of the HCU-3D controller and uses several movement and read out commands.

3.4 Microwave

Using the spin dependent fluorescence of the NV center experimentally often presumes the possibility to individually populate the NV's ground state spin levels. Because of the small energy differences, the transitions between the ground state levels can be driven via a microwave field. All types of experiments including coherent spin manipulations are therefore limited to the possibility to generate and control microwaves deliver it to

²See datasheets on <http://www.smaract.com/>

the sample. In this case, this is achieved via a home-built antenna, consisting of a 30 μm thick gold wire, shortening the inner and outer contacts of an SMA cable. The antenna is connected to a microwave generator (R&S SMF 100A), being able to sweep the microwave frequency in the range of 100 kHz to 22 GHz, allowing for continuous wave electron spin resonance measurements. Adding a fast switch (MiniCircuits ZASWA..) to the microwave electronics also opens the field for pulsed experiments such as the measurement of Rabi oscillations.

3.5 Sample positioning

As the objective is at a fixed position, the sample has to be positioned in the focal spot to acquire an optical image. Having a stable positioning system is advantageous, as it circumvents the need for retracking single emitters during a longer measurement. A well known problem of many piezo positioners is that they suffer from hysteresis effects which result in a drift of the target position. This is problematic for example while using very strong magnetic fields as small drifts in the position already induce a big difference in the magnetic field strength. Initially, the sample was placed on a three axes closed loop stepper system (attocube ECS3030) driven via a USB connected controller (attocube ECC100). The system has a large scan range of $20 \times 20 \times 20 \text{ mm}^3$, allowing for fast high precision positioning of the sample without being affected by the described hysteresis effects. A special advantage over an open loop system is the possibility to save the axes coordinates and thus being able to find single NVs in the diamond again after moving without the need of any structures or marker fabricated into the sample. There were, however, several most hardware issues which made the use of the system impossible. After a short testing period, we switched to an attocube ANSxyz100 piezo positioner, controlled via a instruments PCI-6229 data acquisition card and a digital output rack (NI BNC 2090 A).

4 Results and discussion

4.1 Sample

The NV center is aligned along the $\langle 111 \rangle$ direction of the diamond lattice and can thus point along any of the four equivalent $\langle 111 \rangle$ crystal axes. For purely magnetic interactions of the NV spin with an external magnetic field or adjacent spins, it is irrelevant along which of these four axes the NV center is oriented. However, the use of NV centers in applications such as scanning probe magnetometry or relaxometry requires the possibility to align external magnetic (bias) fields precisely to the quantization axis of NV centers in one given orientation [50]. If all NV centers are equally distributed on the four axes, the maximum fraction of NVs aligned with the external field is 25%. Detection, as well as calibration of an external bias field is achieved using electron spin resonance (ESR) experiments. The signal-to-noise ratio in ESR experiments depends on the ratio of aligned and misaligned NV centers, as the NVs in the misaligned directions add a contribution to the measurement noise. Hence, for an amount of 75% misaligned NVs, the signal to noise ratio drops to a quarter of the value of a single NV, which represents the case where 100% of the NV centers are aligned.

To increase the signal to noise ratio for an NV ensemble, preferential orientation of the NV centers in the diamond would be greatly beneficial. Since most of the NV centers point along a given orientation in a preferentially oriented sample, more than a quarter of the available centers can be used, effectively reducing the noise arising from misaligned NVs in ESR measurements. At the same time, it alleviates the alignment procedures in the case of single NV applications due to the increased chance to find a center in the desired orientation.

Preferential alignment can be achieved by chemical vapor decomposition (CVD) growth of diamond on a $\langle 113 \rangle$ or $\langle 111 \rangle$ oriented substrate [51]. In contrast to growth on a $\langle 111 \rangle$ oriented diamond substrate, thick layers of stress-free diamond can be grown on a $\langle 113 \rangle$ surface [52]. Moreover, the doping efficiency is said to be higher for this orientation and at least partial preferential orientation ($\sim 75\%$) is possible in this configuration [51, 52]

To this end, CVD diamond growth has been performed by Alex Tallaire et. al. at LSPM Villetaneuse on a $\langle 113 \rangle$ oriented optical grade diamond substrate (surface area of about $3 \times 3 \text{ mm}^2$ and a thickness of $500 \text{ }\mu\text{m}$) provided by Element Six. Despite its orientation, the substrate was initially grown in the $\langle 100 \rangle$ direction, and then cut in order to expose the $\langle 113 \rangle$ surface. Above the thick undoped layer, a 50 ppm N doped layer was grown. Such a sample could be used for example in wide-field magnetometry, providing high fluorescence intensity and a close proximity between sample and probe, if the substrate is removed and the the sample is illuminated from the backside. A sketch

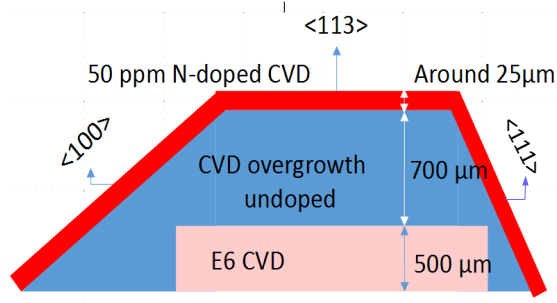


Figure 11: Cross section of the Sample. The area of the $\langle 113 \rangle$ area is reduced compared to the area of the substrate due to the appearance of the $\langle 100 \rangle$ and $\langle 111 \rangle$ facets at the edge of the diamond. *Source:* [52]

of the sample cross-section is shown in Fig.(11).

The sample, as it was used in our experiments, has not been subject to any manipulations as polishing, laser cutting, annealing or chemical treatments. Hence, the NV centers in the N-doped CVD layer exclusively result from the growth process. Typically, the NV density in a CVD doped diamond is not particularly high, because of the low concentration of vacancies in the lattice, which have to be induced for example by electron irradiation [53]. In this sample, however, the NV density was surprisingly high, as can be seen from the PL analysis of the Villetaneuse group [52] and investigating the sample in our experiments shows an extremely high photon count rate of several million counts per second, even for excitation powers of a few micro Watt. As the NV centers entirely lie in the highly doped layer, it is of importance for purposeful fabrication to know the effective thickness of the NV layer. To measure this, we performed a vertical scan through the surface of the diamond (See Fig.(12)). The bright fluorescence area was averaged along y and subsequently fitted with the sum of two Gaussian peaks. The width of the NV layer can be determined as the full width at half maximum (FWHM) of the resulting fit, $w_{NV} \approx 9.6 \mu\text{m}$. Rescaling this value with the refractive index of diamond $n_d = 2.44$ to compensate for the refraction of the beams further into the diamond, the thickness of the NV layer can be determined as $W_{NV} = w_{NV} \cdot n_d \approx 23.42 \mu\text{m}$. This is in reasonable agreement with the estimation given by the Paris group.

To prove that there is at least some preferential alignment of the NV center in the sample, we performed ESR measurements in the regime of weak magnetic field. Since the projection of the field varies for the different orientations, their energy levels will split up by a different amount. From the contrast of the according dips, a statement

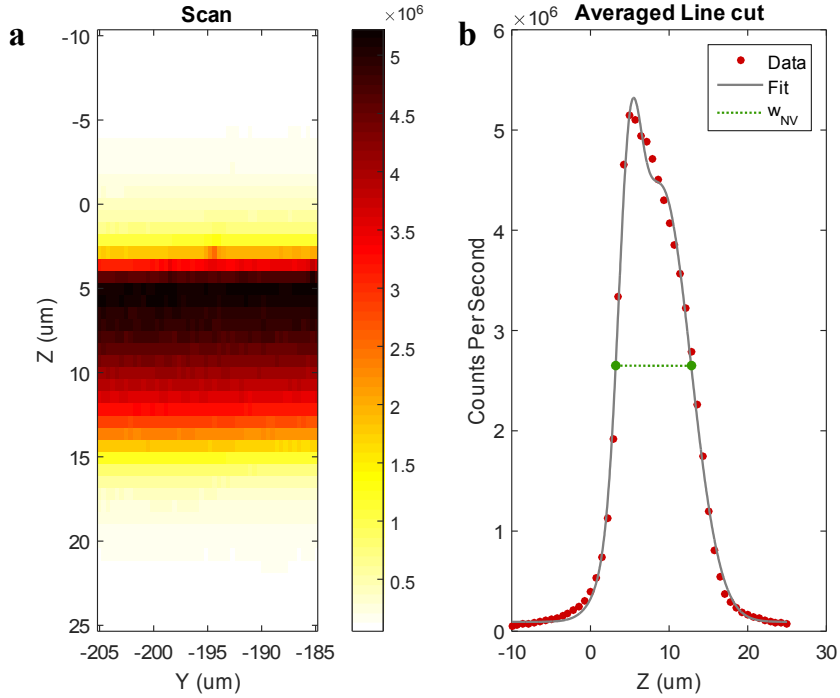


Figure 12: **a** Vertical scan through the sample. The black area indicates the highest photon count rate. The distances on both axes are directly read out from the attocube ECS3030 scanner and refer to the actual travel distance of the stage. **b** Averaged line cut of the scan. The fluorescence was summed along Y and divided by the number of columns. The data was fitted with the sum of two Gaussian peaks (grey line). The FWHM (green line) of the resulting curve, rescaled with the refractive index of diamond, $n_d = 2.44$ gives an estimation of the real NV layer thickness and was determined as $W_{NV} = w_{NV} \cdot n_d \approx 23.42 \mu\text{m}$.

about the alignment can be deduced. If the NVs were equally distributed among the four orientations, the ESR contrast would decrease to a quarter of the value of a single NV (corresponding to 100% orientation in a given direction), as described above. For a single NV, we would expect an average contrast of about 20% in our setup. So a contrast of more than 5% means that the percentage of the NVs in the corresponding orientation is larger than 25%. As the transitions we used showed a contrast of around 9-12%, we assume a NV percentage of $\sim 50 - 60\%$ in this orientation. Fig.(13a) shows three pronounced dips for each of the $|0\rangle \rightarrow |-1\rangle$ transitions (left three peaks) and the $|0\rangle \rightarrow |+1\rangle$ transitions (right three peaks), each one belonging to one orientation of the NV centers. The dips corresponding to the fourth direction is assumed to have too low contrast to be clearly resolved. The ratio of the contrasts of the dips in Fig.(13a) can be used to give an estimation of the percentage of preferential alignment. Normalized to the smallest dip, the contrast ratio is 4.28:2.00:1.00. From this we estimate a preferential

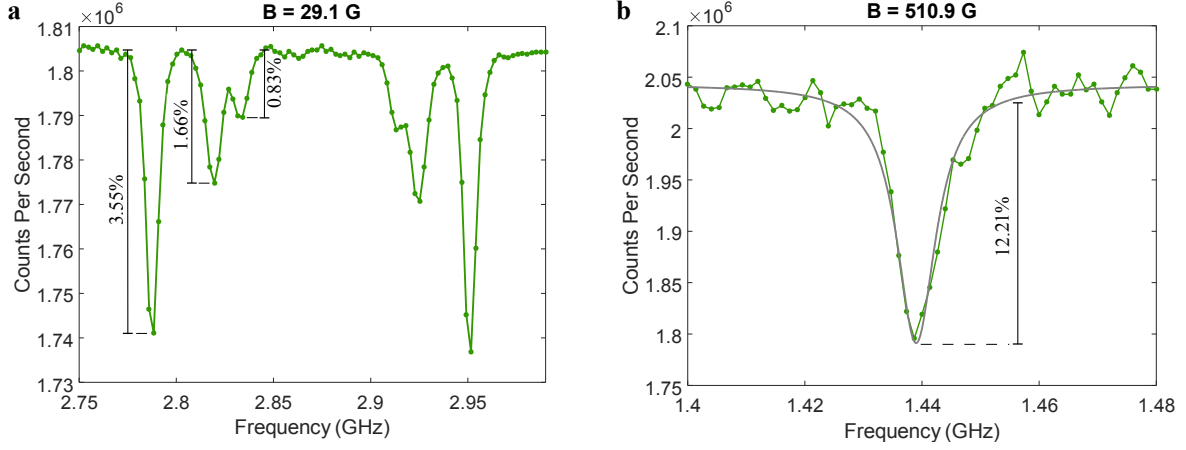


Figure 13: **a** ESR spectrum at ≈ 30 G. The three peaks belong to the $|0\rangle \rightarrow |\pm 1\rangle$ transitions. Each dip belongs to a given orientation of the NV centers. The contrast for each dip in the left triplet is given. From the ratio of the contrasts, an estimation about the percentage of the preferential alignment can be done, as described in the text. The green line is a guide to the eye (Data taken by P. Maletinsky). **b** ESR transition of the dip with the largest contrast at high field. The contrast is over 12% in this case, indicating a preferential alignment of about 60%. The grey line is data fitting with a Lorentzian function.

alignment of 58.76% for the orientation related to the dip with the highest contrast. However, this ratio is not necessarily representative, as the contrast depends on how well the microwave is optimized to the respective orientation. To give a more sophisticated description, the contrast for each dip would have to be measured separately with the micro wave optimized for the corresponding NV centers.

Fig.(13b) shows the transition of the dip with the largest contrast, at an external magnetic field of 510.9 G. The NV centers of the measurement in Fig.(13b) are tilted by an angle of $\sim 30^\circ$ with respect to the $\{113\}$ direction. The dip shows a contrast of 12.21%. Assuming 5% contrast for an equal distribution of the NVs, as described above, preferential alignment of 61.05% can be deduced from this measurement. This is in good agreement with the estimation deduced from the data in Fig.(13a).

The dephasing time T_2^* is a measure for the interaction strength of the NV spin with its environment. The effective field at the location of the NV is not comprised of the external part alone, but also experiences a shift due to the spins in the vicinity of the NV. The transverse magnetic field components that arise due to this shift induce the NV spin to precess around the effective field with the Larmor frequency, effectively causing the spin to dephase. The shift in magnetic field is proportional to the number of the surrounding spins. Hence, a short T_2^* suggests a large number of spins in the environment. Note, that the number of spins includes NV centers as well as P1 centers or nuclear spins.

As described in chapter 1.2.2, $\Gamma_{2,NV}^*$ can be measured via the Ramsey sequence. Fitting the resulting signal with eq.(8) yields both T_2^* and ϵ . This is shown in Fig.(14). This fit yields $\epsilon \sim 1.5$, which indicates that both electronic and nuclear spins contribute approximately equally to the dephasing rate. The For $T_2^* = 160.8 \mu s$, the dephasing rate can be determined as $\Gamma_{2,NV}^* \approx 6.22$ MHz.

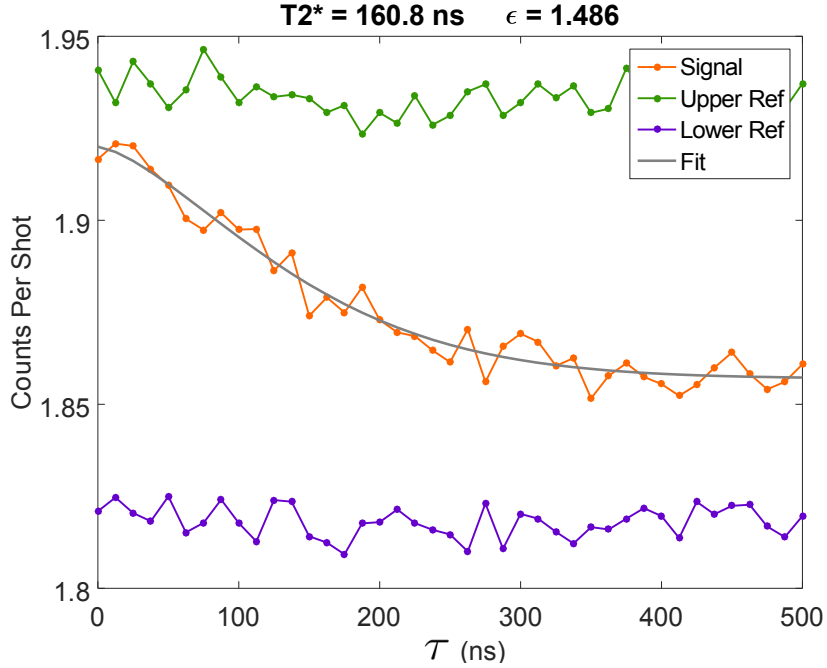


Figure 14: Measurement of T_2^* via the Ramsey sequence. The gray line is fitting the signal (orange line) using eq.(8). The upper (green) and lower (purple) lines serve as a reference and correspond to the signal arising from the $|0\rangle$ and the $|-1\rangle$ states, respectively.

4.2 Magnetic field control

As introduced in the theory section, it is crucial for our measurements to have precise control over the external magnetic field applied to the sample. In our approach, we attached a permanent magnet to a 3 axes closed loop system by SmarAct. Being a problem in terms of stability of the magnet on the one hand, the transverse magnetic field dependence of the NV photoluminescence is on the other hand exploited for the alignment of the magnet of the NV axis. As introduced in section 1.1.2, the PL drops drastically for strong transverse external magnetic fields, but remains bright for fields being perfectly aligned to the NV axis. This can be used to measure a PL map of the NV center as a function of magnet position. The photon count rate is plotted versus the displacement from the starting position in both x and y direction.

As the NV centers lie in the $\{111\}$ plane of the diamond lattice, while most diamond

samples have surface orientations at an angle to this, the surface normal of the magnet has to be at the same angle as the NV to ensure the scanning plane to be perpendicular to the NV axis. So aligning the magnet to the NV centers requires knowledge about the surface orientation of the sample to be able to calculate the angle θ at which the NVs reside in the diamond.

The angle between two crystallographic planes can be calculated as

$$\cos(\theta) = \frac{h_1 h_2 + k_1 k_2 + l_1 l_2}{\sqrt{h_1^2 + k_1^2 + l_1^2} \sqrt{h_2^2 + k_2^2 + l_2^2}} \quad (15)$$

where h_i, k_i, l_i are the Miller indices describing the planes. For the preferentially aligned NV centers in the 113-sample the angle is $\theta_{113} = 29.5^\circ$. Since the stage has no rotational degree of freedom, the angle is applied by moving it proportional $\sin(\theta_{113})$ along y and $\cos(\theta_{113})$ along z when stepping to the next scan line. For high enough fields, the misaligned field components of the external field become high enough to efficiently quench the NV fluorescence, which results in a bright spot in the PL map where the field is aligned (see Fig.(15)). The map is smoothed afterward, by adding the value of 9 points (one point and 8 nearest neighbors) at a time together to have a cleaner picture of the intensity distribution.

The position of the peak is read out afterward and the stage moves to the according coordinates. As can be seen in Fig.(15), the peak is now in the center of the scan, which means that the field is aligned with the NV axis. The precision of the alignment depends on the size of the scan and the number of points. Close to resonance, good results could be achieved using a scan range of $800 \times 800 \mu\text{m}$ and 121 scanning points. This method avoids fitting the intensity distribution and reading out the peak position of the fit, as the determination of the peak position is precise enough for the carried out experiments.

Increasing the field strength close to 512 G narrows the alignment spot since the system starts getting into resonance with the excited state level anti-crossing, as described in section 2.1.2. Further increasing the field shifts the system over the resonance point, and the spot becomes broader again. Fig.(15) shows data for the low field regime and the alignment spot has a width of $\sim 3000 \mu\text{m}$. For data taken around 512 G, the bright spot only has a width of $\sim 300 \mu\text{m}$ (data not shown).

Measuring T_1 spectra with high enough resolution requires the calibration of a few hundred magnetic field points. This procedure is automated and integrated in the MATLAB control GUI designed for this purpose and first calibrations included an alignment scan as well as an ESR measurement for each point. The applied magnetic field can be deduced from the ESR transition frequency as follows:

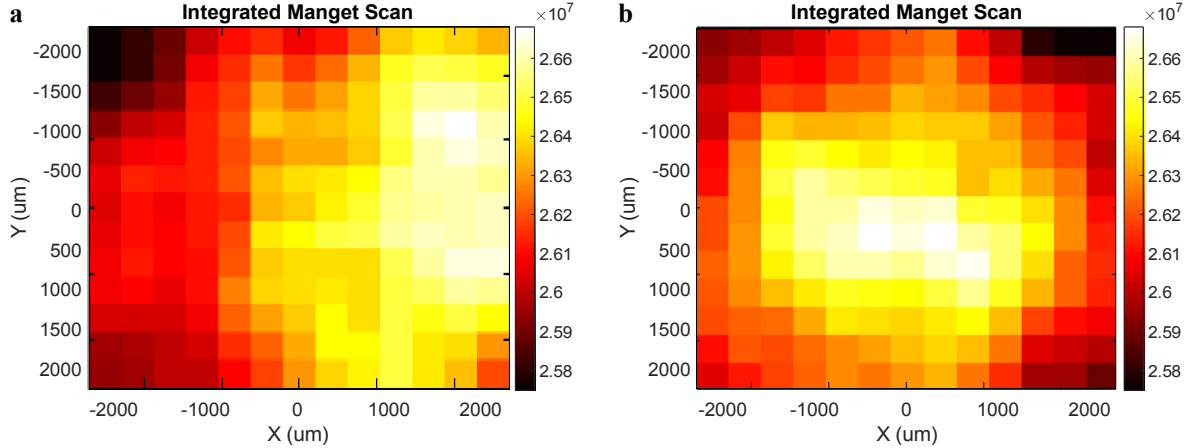


Figure 15: Magnet scans at low magnetic field before (a) and after (b) the alignment procedure. The PL is measured for every position of the magnet. Afterward, the scan is integrated as described in the text. The maximum PL in a is read out and the stage subsequently moves to the according position. The external field is then aligned to the NV axis and the maximum in the second scan in b is centered

$$B_z = \frac{(\omega_0 - \omega)}{\gamma_{NV}} \quad (16)$$

where $\omega_0 = 2.87$ GHz is the zero field transition of the NV and ω is the measured transition frequency in the ESR experiment. Recent results on spin wave imaging [54] with a similar technique shows, that it is possible to find a field configuration that can be approximated by a straight line. As can be seen from Fig.(16), our data shows the same behavior in the given field range. Knowing this, the time needed for the calibration procedure can be strongly contracted by reducing the number of alignment scans (only every fifth point in our latest run) during the calibration.

The precision with which the magnetic field can be determined mainly depends on how well the ESR signal can be fitted. To optimize the fit procedure, we dynamically adjust the ESR frequency range in a feed-forward loop, such that it covers a range of ± 10 MHz around the transition frequency. The range for the upcoming measurement is calculated with respect to the central frequency of the fit to the current one.

4.3 Magnetic resonance

Being equipped with a precisely calibrated magnetic field and all optical read-out of the T_1 time of the NV, the road for the detection of magnetic resonances at the nano scale is paved. The target system for our measurements are the free electrons arising from P1 centers in the diamond lattice, which consists of a nitrogen atom at a carbon lattice

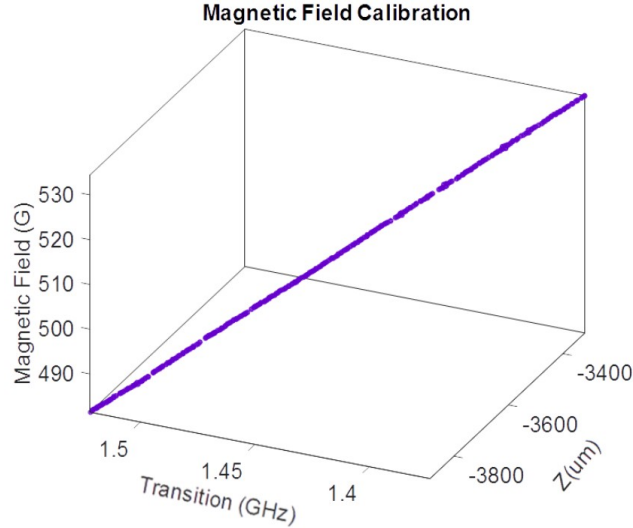


Figure 16: Magnetic Field Calibration. The magnetic field along the NV axis depends linearly on both the transition frequency and the position of the magnet. Jumps in the calibration are due to inaccuracies in the fit.

site. Unlike the NV center, the P1 is completely surrounded by carbon atoms and is not coupled to a vacancy. Hence, the access electrons form donor levels in the conduction band [55] which is then able to be coupled to the NV spin. Because it doesn't have a zero field splitting along a given quantization axis, the P1 electron is not aligned along a special orientation in the diamond lattice. Rather than that, it aligns along the external magnetic field, which, in turn, is aligned with the NV axis. We can therefore think of the P1 center lying in the $\{111\}$ direction.

To measure T_1 , we used the sequence described in the theory section. To have a first idea of the amount by which T_1 will be reduced at resonance, we measured the full decay for different magnetic fields. The first measurement was done far away of any resonance, whereas the second one was performed at 512 G, where the system is supposed to be in resonance with the surrounding electronic spins. The data is shown in Fig.(17). The experiment was done using the T_1 sequence described in the theory part (purple data in Fig.(17)). In addition, the same experiment was done including a π pulse at the end of the wait time before read out (yellow data in Fig.17). Subtracting the two signals eliminates all contributions that don't correspond to the NV spin relaxation. The reduced signal is subsequently fitted with a single exponential decay, giving T_1 of the relaxation process. The difference between the normalized exponentials for the on and off resonance relaxation is shown in Fig.(17b). T_1 is reduced from ~ 5.2 ms to ~ 1.5 ms, which is an amount of $\sim 28\%$, when the system is in resonance with environmental spin transitions. This is the maximum contrast to be expected for a resonance dip in the T_1 spectrum.

Measuring magnetic resonance spectra as described in section 1.2.3 would require the measurement of a full T_1 decay for all points of the magnetic field configuration. To shorten the time needed for the experiment, we only read out the fluorescence for a few values of τ instead of measuring the whole relaxation.

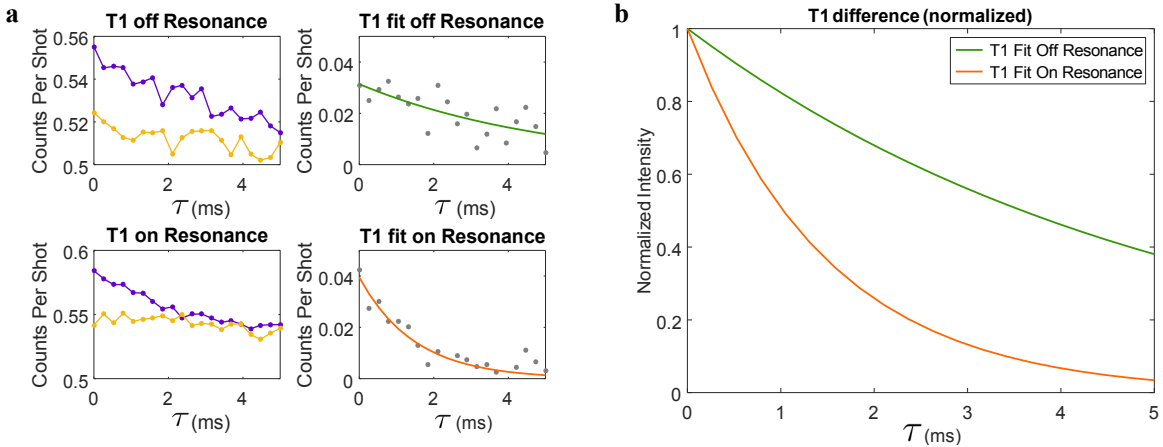


Figure 17: **a** T_1 measurements on and off resonance. The left column shows the measurement with the NV being initialized in $|0\rangle$ (purple) and $|-1\rangle$ (yellow). The two measurements are subtracted (gray dots in right column) to omit contributions other than from the NV spin. The subtracted signal is fitted with a single exponential decay (green and orange curves in right column). **b** Normalized fit functions from **a**. Due to the faster decay, the fluorescence for a given time is decreased in contrast to the off resonance case. The maximum contrast is $\sim 28\%$.

Due to the reduction of T_1 at resonance, the count rate for a given time is reduced compared to the off resonant case. Monitoring the count rate as a function of the external magnetic field, thus allows for a fast, robust read out the reduction of T_1 . In addition, we slightly modified the read out scheme (see Fig.(18a)): While the read out laser is on, we apply two short read-out pulses, one at the beginning of the laser pulse and one at the end. The first pulse provides information about the population in the $|0\rangle$ state after a given decay time, resulting in a reduced photon count rate I_s . At the end of the laser pulse, the NV is reinitialized in the $|0\rangle$ state and the second measurement thus serves as reference count rate, I_r , and is used to normalize the signal. This was done for five different values of τ from 0-1200 ns. Again, the experiment was repeated with a π pulse before read out to exclude all environmental contributions (See Fig.(18c)). The data was subsequently subtracted as described above, normalized to the signal at $\tau = 0$ ns (orange curve in Fig.(18a)) and fitted with five Lorentzian functions Fig.(18f). The spectra were measured for a magnetic field configuration of 300 points from ~ 480 -534 G and are shown in Fig.(18). Fig.(18f) shows the T_1 spectrum for adjacent P1 centers. The main dip at ~ 512 G is accompanied by four narrow side transitions. These

transitions are characteristic for the P1 center and can be explained as follows. There are two effects contributing to the appearance of the five dips. On the one hand, the P1 center electrons exhibit a hyperfine triplet, due to the coupling to the P1's nitrogen nuclear spin. The main dip corresponds to the $m_I = 0$ spin projection, whereas the two transitions corresponding to $m_I = \pm 1$ occur at higher ($m_I = -1$) or lower ($m_I = +1$) fields, respectively.

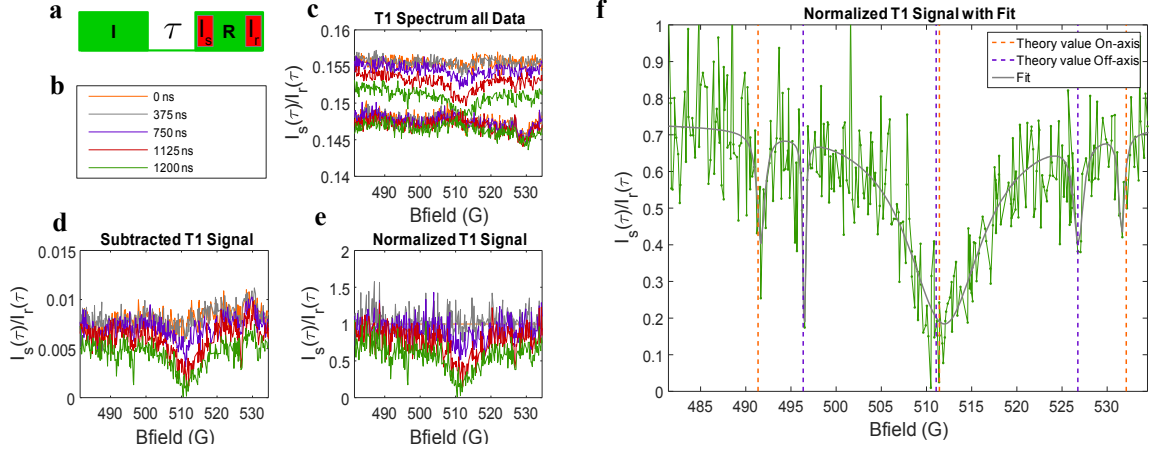


Figure 18: **a** T_1 sequence used for the measurement. During the read out pulse, two measurements are applied. The first pulse I_s measures the population in the $|0\rangle$ state after a given τ , the second pulse I_r serves as a reference measurement and is used to normalize the signal. **b** Legend for **c-f**. **c** Full spectrum. The upper five lines refer to initialization in $|0\rangle$, the lower five to $|-1\rangle$. The asymmetry is due to imperfect initialization due to a mismatch of either the length or the frequency of the π pulse that brings the NV from $|0\rangle \rightarrow |-1\rangle$ **d** Subtracted signal. The measurements for both initializations have been subtracted to isolate the NV signal. **e** Normalized spectra. All spectra have been normalized to the subtracted signal at $\tau = 0$ ns. **f** Magnetic resonance spectrum at $\tau = 1200$ ns. At 512 G, the system is in resonance with all electronic spins in the environment. The four side dips are due to the different hyperfine splitting of on-axis and off-axis P1 centers (see text). The gray line is data fitting with 5 Lorentzian functions, the purple and orange dashed lines indicate the theoretical values of the transitions according to [20]

On the other hand, there are two possibilities how the P1 can be oriented with respect to the NV. The symmetry axis of the P1 electron can be parallel with the NV axis ('on-axis'), or along one of the other three axes lying in the $\{111\}$ direction, namely $[\bar{1}11]$, $[1\bar{1}1]$ and $[11\bar{1}]$ ('off-axis') [20, 56, 57]. Due to this different orientation, the on-axis and off-axis P1 centers have different hyperfine splittings, resulting in a total of five dips. The dashed line in Fig.(18f) indicate the theory values for the transitions according to [20]. The data matches the theory very well (deviations $\lesssim 8.3\%$) and full T_1 measurement at each side dip position confirmed that we observed an actual dip rather than measurement

noise (data not shown). Note, that also for the off-axis P1 centers, the $m_I = 0$ transition belongs to the central dip. The appearance of five dips is not, as may be expected, an ensemble effect. Since every P1 center switches between all four symmetry axis on a time scale of a few ms, also a single P1 would exhibit five transitions in the spectrum for long enough overall measurement times.

4.4 Estimation of P1 density

The long T_1 on resonance suggests that the P1 density in the sample is comparatively low. Therefore, it is useful to give an estimation about the P1 density. For nuclear spins, where the interaction does not drop off too fast with distance, we could make use of eq.(14), which describes the decay rate in resonance with a nuclear spin. As a first step, we try an analog procedure with eq.(13). This requires the measurement of the full decay rate $\Gamma_{2,\text{tot}}^*$. Since the dephasing rate of the P1 electrons can not be measured, we assume $\Gamma_{2,\text{tot}}^* = 2\Gamma_{2,\text{NV}}^*$. This makes sense, since both systems are electronic spins, which should have a similar dephasing rates.

Eq.(13) describes the coupling to a single spin. However, all P1 centers contribute to the full relaxation rate. Instead of summing over discrete contributions, we introduce an average P1 density ρ_{P1} and integrate over the volume:

$$\begin{aligned}
\Gamma_{1,\text{tot}} &= \int_{\text{dV}} \Gamma_{1,\text{res}}^i \rho_{P1} \\
&= \int_0^{2\pi} \int_0^\pi \int_{r_{\text{min}}}^\infty \frac{1}{\Gamma_{2,\text{tot}}^*} \underbrace{\left(\frac{\mu_0 \gamma_{\text{NV}} \gamma_{P1} \hbar}{2\sqrt{2}} \right)^2}_{:=\Lambda} \left(\frac{3\sin^2(\theta)}{r^3} \right)^2 \rho_{P1} r^2 \sin(\theta) dr d\theta d\phi \\
&= \frac{32\pi\Lambda}{5r_{\text{min}}^3} \frac{\rho_{P1}}{\Gamma_{2,\text{tot}}^*}
\end{aligned} \tag{17}$$

where Λ is constant. Solving eq.(17) for ρ_{P1} and writing $\Gamma_{2,\text{tot}}^* = 2\Gamma_{2,\text{NV}}^*$ yields

$$\rho_{P1} = \frac{10r_{\text{min}}^3}{32\pi\Lambda} \Gamma_{1,\text{tot}} \Gamma_{2,\text{NV}}^* \tag{18}$$

As ρ_{P1} is an average density of P1 centers, the value of r_{min} has to be chosen as the radius for the closest-possible distance to a P1 center, which is one bond-length of two carbon atoms in the diamond lattice. Using this, as well as the values for $\Gamma_{1,\text{tot}}$ and $\Gamma_{2,\text{NV}}^*$ as given above, the average P1 density would be way out of any sensible range.

The reason for this problem is most likely due to the fact that the interaction with electrons can be assumed to be strong for the few first neighbors, but drops off very fast with increasing distance to the NV. To overcome this problem, there it would require to establish a term that regulates the interaction with the distance, which occurred to be difficult in an analytic description. Rather than that, the P1 density could be estimated numerically.

To this end, we define a number of electronic spins as nearest neighbors, arranged in a diamond lattice. For the interaction with each spin we employ eq.(13) for a short time. This gives the probability for a flip flop between the two spins. Applying the interaction for a short time and jumping from one neighbor to the next gives a decay signal which can be compared to the data after integration. Successively changing the number of nearest neighbors allows to estimate the P1 density. The calculations are still in progress.

5 Summary and outlook

NV centers in nanostructures suffer from increased decoherence. A proper means to investigate the origin of this effect, is T_1 relaxometry using an NV spin to detect magnetic resonance spectra of NV centers environment. To this end, we equipped a room temperature scanning confocal microscope with the components to investigate the environment of the NV at the nanoscale. We exploit the magnetic field dependent photoluminescence to align the external magnetic field to the quantization axis of the NV center. Calibration of the field strength as a function of the position is fully automated and implemented in the control software.

To increase the signal to noise ratio in ESR experiments which are used to measure the magnetic field for example in scanning probe magnetometry, preferential orientation of the NV centers is highly desirable. It has been shown that preferential orientation of NVs is possible in $\{113\}$ oriented diamond, preserving efficient CVD growth of the diamond. The sample provided by our partners in Paris was grown in that manner and characterized during the thesis. The thickness of the NV containing layer has been determined to be $W_{NV} \approx 23.42 \mu\text{m}$, which is in reasonable agreement with the estimation of $25 \mu\text{m}$ given by Paris. Preferential orientation of the NV centers of $\approx 60\%$ could be confirmed using electron spin resonance experiments.

To confirm the functionality of the setup, we performed paramagnetic resonance experiments around 500 G, using the P1 center as target spin. The characteristic spectrum of the P1 centers was observed. The noisy signal resulting from a relatively high T_1 time at resonance indicates a relatively low density of P1 centers. The calculation to estimate the P1 density in the sample is still in progress.

After paving the road for magnetic resonance spectroscopy in nanostructures, the most consequent step would be to characterize scanning probe samples used in our labs, both for electronic and nuclear target spins. Correlating noise spectra with T_2 times of single NVs in pillars could yield information about spin and charge distributions in the vicinity of the NV as a result of the fabrication process. Nuclear magnetic resonance experiments together with surface treatments could help to factor out the influence of nuclear spins at the surface.

6 Acknowledgments

I want to thank Prof. Patrick Maletinsky warmly for the possibility to perform this thesis and my whole master's in his group, for the supervision and the patience with all kind of delays and problems. Also, special thanks go to Dr. James Wood and Lucas Thiel for more supervision, for the endurance with my questions and a lot of help with the experiment, data evaluation, programming and eventually the writing of the thesis. Last but not least i want to thank all the remaining, new and former members of the quantum sensing group for many fruitful discussions and a helping hand in the lab. I had two awesome years!

7 APPENDIX

7.1 A: Description of LaserPower GUI

All experiments in the group are controlled via MATLAB, having several graphical user interfaces (GUIs) providing relatively easy to use surfaces without the need of intense programming knowledge. Controlling the AOM setups, however, was done by single commands and running separates scripts from the MATLAB command line without having a GUI for it. As the setup was built up from scratch during the thesis and every other experiment of the group uses such an AOM setup to modulate the excitation beam, it made sense to create a GUI to enable easier control of these parts. The surface of the GUI is depicted in Fig.(19). As can be seen, it consists of three parts: A simple laser power control panel, a power calibration panel and a panel to measure saturation curves of NV centers. The MATLAB code behind the GUI is generally uses only one script, which is called ‘ao_goto’, to communicate with the NI hardware that controls the voltage output delivered to the AOM setup. ao_goto is written by Sungkun Hong and has the analog output channel number of the NI box and the desired voltage value as input variables. MATLAB- wrapper files contain the commands to apply the desired voltage to the selected output channel.

The laser power control panel provides a simple arrangement of a few buttons and input fields to set an arbitrary DC voltage between 0 and 3.6 V (limit of the AOM), to step the voltage in variable steps, to turn the laser on and off, and to update the displayed voltage value. The scroll down menu labeled ‘Channel Control’ enables selection of the output channel to which the switch in the AOM setup is connected. The second part, the Laser Power Calibration panel, is included to handle the power control via a power calibration curve. The curve shows the voltage dependence of transmitted power of the AOM, which is saturating for a given value and follows a curve rather than a linear behavior. In principle, the power dependence could be automated by inserting a photo diode at some point in the experiment and read out the generated voltage via a connection to the NI box. However, at the moment, the power has to be measured by hand via a power meter and typed into the input field. The ‘Next’ and ‘Prev’ buttons allow to move along the calibration curve. The voltage indicated by the blue diamond marker is directly applied to the AOM. The ‘Plot’ button plots the input values of the power versus the calibration voltages. As it is given by the characteristics of the AOM, variations in the input laser power change only the amplitude of the calibration curve while the shape stays the same. Knowing the power calibration is on the one hand side important to make sure not to damage the AOM by driving it with too high power and on the other hand side to be able to measure the excitation power dependence of the NV fluorescence,

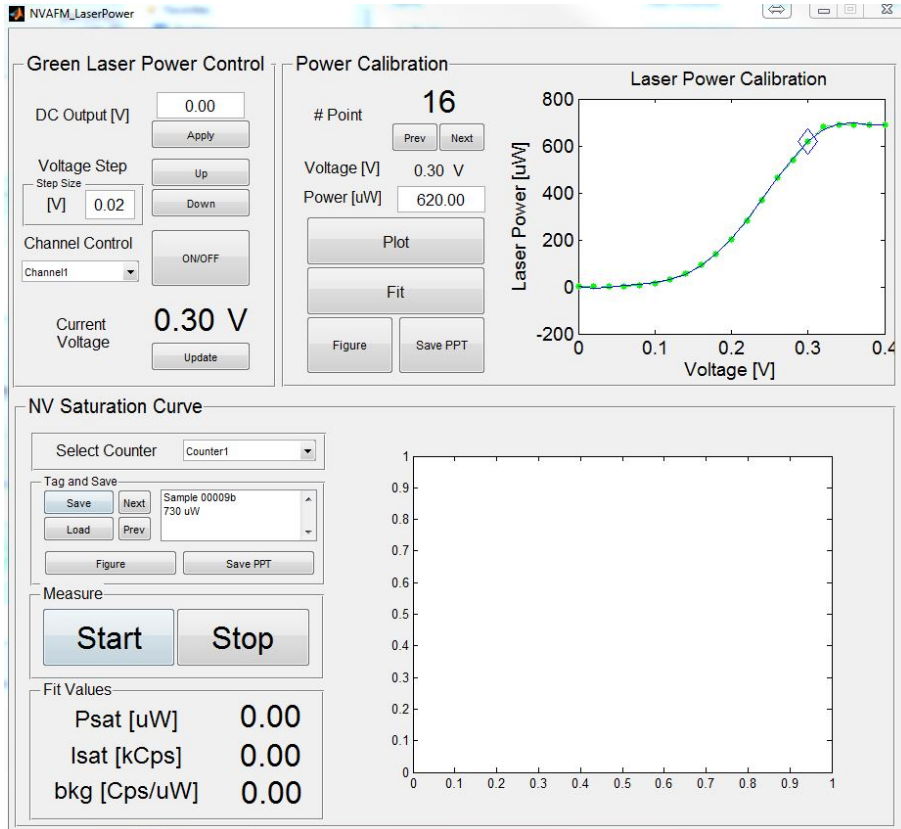


Figure 19: Screenshot of LaserPower GUI. The GUI was created to control the AOM setup which modulates the excitation laser beam. (upper left panel). It is also capable of calibrating the Power dependence of the Laser as a function of the Voltage amplitude applied to the AOM (upper right panel). In addition, a function to measure saturation curves of the NV is implemented (lower panel)

which can be done by the third part, the Saturation Curve panel. To that end, it is useful to fit the measured calibration with a 6th order polynomial, which is afterward used as input axis in the Saturation Curve panel. The fitting is automatically done by hitting the 'Fit' button. The fluorescence of an NV center depends on the input power P and saturates after a linear period. This behavior can be modeled by simply solving the rate equations of the NV center [58]. Characteristic properties are the saturation power P_{Sat} , the saturation intensity I_{Sat} and the background signal b , which shows a linear behavior. NV saturation curves can be a helpful tool, as it gives information either on how well the setup is aligned (provided the NV characteristics are known), about the nature and the quality of the implanted NV centers (given the setup can be assumed as well aligned) or on the efficiency of photonic nano structures [59]. The script to measure saturation curves was amongst others written by Lucas Thiel and is implemented in the code for the Laser Power GUI. As input voltages, the fit of the power calibration curve is used. The input range can be determined by moving around on the calibration

curve. The location of the blue diamond marker sets the maximum value of the input range while the lower value is always zero. The ability of setting the upper value in this way is to avoid the application of the highest few points of the calibration curve, which usually saturate around a certain value for some input voltages. Measuring NV saturation curves, this would yield in aberrations from the correct NV behavior. The curve is measured by applying the voltages given by the input values and measure the fluorescence of the NV. Once the measurement is taken, the data is automatically fitted using the following equation:

$$I(P) = \frac{I_{sat}}{1 + \frac{P_{sat}}{P}} + b \cdot P \quad (19)$$

The fitted values for P_{Sat} , I_{Sat} and b are displayed in the GUI and the plot on the right side contains the measured signal (red stars), the fit to the data (black dots), the linear background signal (green dashed line) and the actual NV signal (blue diamonds), calculated from the fit by subtracting the background in each point from the measured signal. The scroll down menu labeled ‘Select Counter’ allows for selection of the detection instrument used to collect the NV fluorescence. The ‘Start’ and ‘Stop’ buttons run and stops the script described above to measure the saturation curves. The data can be tagged and saved in the according areas in the panels and the figures can be saved in a power point file via the ‘Figure’ and ‘Save PPT’ buttons.

7.2 B: Description of MagnetPositioner GUI

Since the external magnetic field at the sample depends on the relative position of the magnet and the sample, it is vital for the experiments to calibrate the magnetic field strength as a function of the magnet position. Tis calibration is used as input axis for the measurement of T_1 spectra. Also this GUI is arranged in panels.

The first panel is called ‘Alignment’. The input fields can be used to set the scan range, the number of points in the scan, as well as the angle at which the plane is scanned with respect to the sample surface. The ‘Set Scan’ button generates the scan values and the values for the plot window. After pressing ‘Align’, the alignment scan is performed as described in chapter 4.2. The read out time gives the time for each pixel can be adjusted in the according input field.

The ‘Adjust B’ button runs a script that automated this calibration within a given range set by the ”Set Lower” and ”Set Upper” buttons. To make proper use of this, the lowest (highest) field strength has to be selected by moving the magnet close enough to the diamond and measure the applied field via an electron spin resonance (ESR) experiment. Aligning the magnet and hitting the ”Set Lower” (”Set Upper”) button

saves the coordinates of the stage. The number of calibration points, according to which the step size of the magnet in the direction from the lower reference to the higher one is calculated, can be entered at the lower right input field of the Alignment panel. The code then aligns the magnet for each calibration point, measures an ESR spectrum, determines the transition frequency and the associated field strength out of the Lorentzian fit to the dip in the spectrum (ESR experiment, f.ex in [28]) and saves them together with the stage coordinates in a MATLAB struct. The data for each scan is saved in a separate folder labeled with the current date. Loading these files provides access to every calibration at a later point to use them, for example, for some post-processing of some data or to repeat the experiment.

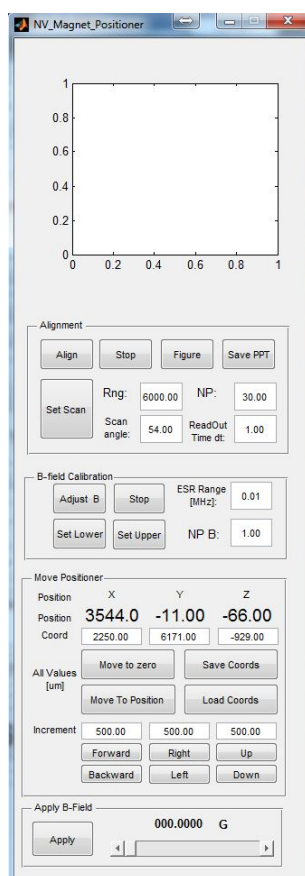


Figure 20: Magnet positioner GUI as described in the text. The GUI was created to move the SmarAct stage for positioning of the magnet, as well as alignment and calibration of the magnetic field with respect to the sample.

The ‘Move Positioner’ panes allows to control the stage via MATLAB. Single steps can be performed, where the ‘Forward’ and ‘Backward’ direction belongs to the x-axis, ‘Right’ and ‘Left’ to the y-axis and ‘Up’ and ‘Down’ to the z-axis of the scanner. The user can also move the stage to desired coordinates via the input fields and the ‘Move to Position’ button. ‘Move to zero’ brings the stag back to the origin of the coordinate system. Even

though this might be set via a command in the library, it can also be done by turning the controller off and on again. The current position is then set to zero. The current coordinates can also be saved and loaded again at a later time point.

The last panel, called "Apply B-field" only contains a slider and a button. The calibrated magnetic field strengths can be selected by the slider and hitting the "Apply" button drives the magnet to the according position. The selected field strength is displayed above the slider and changing the calibration automatically updates the slider.

7.3 C: Description of Spectrum GUI

To measure T_1 spectra, it requires several GUIs with different functions. The magnetic field is calibrated via the magnet positioner GUI, the pulse sequence is generated via the sequence experiment GUI and the data is measured via the pulse blaster GUI. Subsequently, the data has to be read out and post processed. As the spectra employ quite a lot of points, we designed a new GUI called 'NVAFM_Spectrum' which automates the procedure. The surface of the GUI can be seen in Fig.(21)

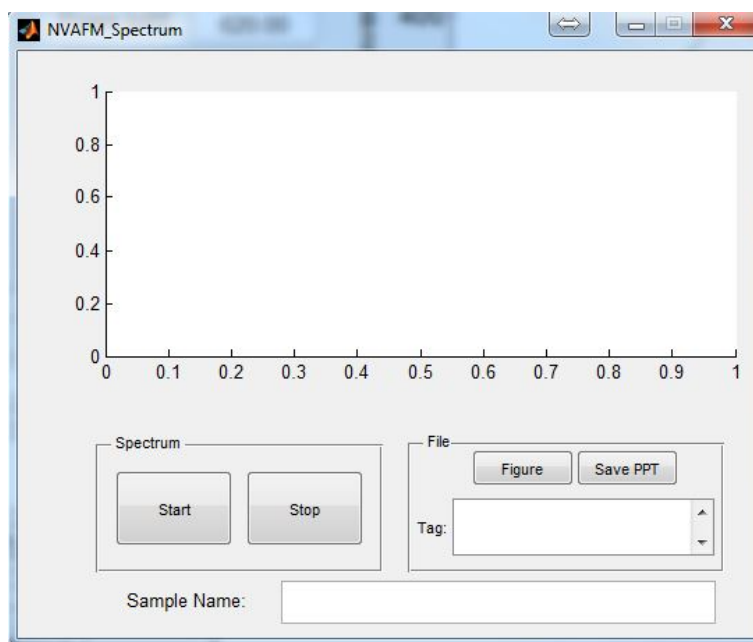


Figure 21: Spectrum GUI. The GUI was designed to automate the measurement process for T_1 spectra.

Besides the 'File' panel which employs the usual functions to save the figure, there is also a input field called 'Sample Name'. This input string will be an appendix to the file name of the automatically saved data, to be able to distinguish between different measurements. The 'Start' and 'Stop' buttons run and stop the measurement, as the name suggests. If a measurement is started, the GUI only executes the start button of the pulse blaster

GUI and moves to the next calibration point of the calibrated magnetic field. All the measurement parameters have to be adjusted in the respective GUIs. The data are automatically read out of smNVAFM_pulse_blast.Counter and processed depending on the calibration of the measurement sequence.

7.4 D: List of figures

1	Schematic of NV center and level diagram	5
2	Field dependence of transition rates	8
3	Misalignment anlage dependence of NV fluorescence	9
4	Working principle of Ramsey sequence	12
5	Phonon induced transition rates	13
6	Working principle of FID sequence	14
7	Influence of ϵ	16
8	Relaxation rates at resonance and MR principle	19
9	Schematic of the Setup	21
10	Principle of confocal microscopy	23
11	Cross section of the sample	27
12	Thickness of NV Layer	28
13	Measurements on preferential alignment	29
14	T_2^* measurement	30
15	Alignment procedure	32
16	Magnetic Field Calibration	33
17	T1 on and off resonance	34
18	T1 Spectra	35
19	LaserPower GUI	42
20	Magnet Positioner GUI	44
21	Spectrum GUI	45

References

- [1] Patrick Maletinsky, Sungkun Hong, Michael Sean Grinolds, Birgit Hausmann, Mikhail D Lukin, Ronald L Walsworth, Marko Loncar, and Amir Yacoby. A robust scanning diamond sensor for nanoscale imaging with single nitrogen-vacancy centres. *Nature nanotechnology*, 7(5):320–324, 2012.
- [2] A Dréau, J-R Maze, M Lesik, J-F Roch, and V Jacques. High-resolution spectroscopy of single nv defects coupled with nearby ^{13}C nuclear spins in diamond. *Physical Review B*, 85(13):134107, 2012.
- [3] F Jelezko and J Wrachtrup. Quantum information processing in diamond. *arXiv preprint quant-ph/0510152*, 2005.
- [4] Chiou-Fu Wang, Ronald Hanson, DD Awschalom, EL Hu, T Feygelson, J Yang, and JE Butler. Fabrication and characterization of two-dimensional photonic crystal microcavities in nanocrystalline diamond. *Applied Physics Letters*, 91(20):201112, 2007.
- [5] Lucas Thiel, Dominik Rohner, Marc Ganzhorn, Patrick Appel, Elke Neu, B Müller, R Kleiner, D Koelle, and P Maletinsky. Quantitative nanoscale vortex imaging using a cryogenic quantum magnetometer. *Nature nanotechnology*, 11(8):677–681, 2016.
- [6] Tobias Staudacher, Fazhan Shi, S Pezzagna, Jan Meijer, Jiangfeng Du, Carlos A Meriles, Friedemann Reinhard, and Joerg Wrachtrup. Nuclear magnetic resonance spectroscopy on a (5-nanometer) 3 sample volume. *Science*, 339(6119):561–563, 2013.
- [7] HJ Mamin, M Kim, MH Sherwood, CT Rettner, K Ohno, DD Awschalom, and D Rugar. Nanoscale nuclear magnetic resonance with a nitrogen-vacancy spin sensor. *Science*, 339(6119):557–560, 2013.
- [8] Alexander Huck, Shailesh Kumar, Abdul Shakoor, and Ulrik L Andersen. Controlled coupling of a single nitrogen-vacancy center to a silver nanowire. *Physical review letters*, 106(9):096801, 2011.
- [9] Gopalakrishnan Balasubramanian, Philipp Neumann, Daniel Twitchen, Matthew Markham, Roman Kolesov, Norikazu Mizuochi, Junichi Isoya, Jocelyn Achard, Johannes Beck, Julia Tissler, et al. Ultralong spin coherence time in isotopically engineered diamond. *Nature materials*, 8(5):383–387, 2009.
- [10] Patrick Appel, Elke Neu, Marc Ganzhorn, Arne Barfuss, Marietta Batzer, Michael Gratz, Andreas Tschöpe, and Patrick Maletinsky. Fabrication of all diamond

- scanning probes for nanoscale magnetometry. *Review of Scientific Instruments*, 87(6):063703, 2016.
- [11] Bryan A Myers, A Das, MC Dartiailh, K Ohno, David D Awschalom, and AC Bleszynski Jayich. Probing surface noise with depth-calibrated spins in diamond. *Physical review letters*, 113(2):027602, 2014.
- [12] Boris Naydenov, Friedemann Reinhard, Anke Laemmle, V Richter, Rafi Kalish, Ulrika FS D’Haenens-Johansson, Mark Newton, Fedor Jelezko, and Joerg Wrachtrup. Increasing the coherence time of single electron spins in diamond by high temperature annealing. *arXiv preprint arXiv:1012.0216*, 2010.
- [13] BK Ofori-Okai, S Pezzagna, K Chang, M Loretz, R Schirhagl, Y Tao, BA Moores, K Groot-Berning, J Meijer, and CL Degen. Spin properties of very shallow nitrogen vacancy defects in diamond. *Physical Review B*, 86(8):081406, 2012.
- [14] T Roskopf, A Dussaux, K Ohashi, M Loretz, Romana Schirhagl, H Watanabe, S Shikata, Kohei M Itoh, and CL Degen. Investigation of surface magnetic noise by shallow spins in diamond. *Physical review letters*, 112(14):147602, 2014.
- [15] B. A. Myers, A. Ariyaratne, and A. C. Bleszynski Jayich. Double-quantum spin-relaxation limits to coherence of near-surface nitrogen-vacancy centers. *ArXiv e-prints*, July 2016.
- [16] DT Edmonds. Larmor precession as a mechanism for the detection of static and alternating magnetic fields. *Bioelectrochemistry and Bioenergetics*, 30:3–12, 1993.
- [17] Paul A. Tipler. *Physik*. Spektrum, 1994.
- [18] Gunnar Jeschke, M Pannier, and Hans Wolfgang Spiess. Double electron-electron resonance. In *Distance Measurements in Biological Systems by EPR*, pages 493–512. Springer, 2002.
- [19] Nir Bar-Gill, Linh M Pham, Andrejs Jarmola, Dmitry Budker, and Ronald L Walsworth. Solid-state electronic spin coherence time approaching one second. *Nature communications*, 4:1743, 2013.
- [20] J. D. A. Wood, D. A. Broadway, L. T. Hall, A. Stacey, D. A. Simpson, J.-P. Tetienne, and L. C. L. Hollenberg. Wide-band nanoscale magnetic resonance spectroscopy using quantum relaxation of a single spin in diamond. *APS*, 94(15), October 2016.

- [21] LT Hall, P Kehayias, DA Simpson, A Jarmola, A Stacey, D Budker, and LCL Hollenberg. Detection of nanoscale electron spin resonance spectra demonstrated using nitrogen-vacancy centre probes in diamond. *Nature communications*, 7, 2016.
- [22] Christoph Schreyvogel, Vladimir Polyakov, Sina Burk, Helmut Fedder, Andrej Denisenko, Felipe Fávoro de Oliveira, Ralf Wunderlich, Jan Meijer, Verena Zuerbig, Jörg Wrachtrup, et al. Active and fast charge-state switching of single nv centres in diamond by in-plane al-schottky junctions. *Beilstein Journal of Nanotechnology*, 7(1):1727–1735, 2016.
- [23] Christoph Schreyvogel, Marco Wolfer, Hiromitsu Kato, Matthias Schreck, and Christoph E Nebel. Tuned nv emission by in-plane al-schottky junctions on hydrogen terminated diamond. *Scientific reports*, 4:3634, 2014.
- [24] P Neumann, R Kolesov, V Jacques, J Beck, J Tisler, A Batalov, Lachlan Rogers, NB Manson, G Balasubramanian, F Jelezko, et al. Excited-state spectroscopy of single nv defects in diamond using optically detected magnetic resonance. *New Journal of Physics*, 11(1):013017, 2009.
- [25] MW Doherty, F Dolde, H Fedder, F Jelezko, J Wrachtrup, NB Manson, and LCL Hollenberg. Theory of the ground-state spin of the nv- center in diamond. *Physical Review B*, 85(20):205203, 2012.
- [26] L Childress, MV Gurudev Dutt, JM Taylor, AS Zibrov, F Jelezko, J Wrachtrup, PR Hemmer, and MD Lukin. Coherent dynamics of coupled electron and nuclear spin qubits in diamond. *Science*, 314(5797):281–285, 2006.
- [27] Michael SJ Barson, Phani Peddibhotla, Preeti Ovarthaiyapong, Kumar Ganesan, Richard L Taylor, Matthew Gebert, Zoe Mielens, Berndt Koslowski, David A Simpson, Liam P McGuinness, et al. Nanomechanical sensing using spins in diamond. *arXiv preprint arXiv:1612.05325*, 2016.
- [28] Lucas Thiel. *Spin Coherence in Nitrogen-Vacancy Centers*. Master thesis, Uni Basel/Harvard University, 2014.
- [29] Lilian Isabel Childress. *Coherent manipulation of single quantum systems in the solid state*. Dissertation, Harvard University, 2007.
- [30] NB Manson, JP Harrison, and MJ Sellars. Nitrogen-vacancy center in diamond: Model of the electronic structure and associated dynamics. *Physical Review B*, 74(10):104303, 2006.

- [31] LJ Rogers, RL McMurtrie, MJ Sellars, and NB Manson. Time-averaging within the excited state of the nitrogen-vacancy centre in diamond. *New Journal of Physics*, 11(6):063007, 2009.
- [32] JP Tetienne, L Rondin, P Spinicelli, M Chipaux, T Debuisschert, JF Roch, and V Jacques. Magnetic-field-dependent photodynamics of single nv defects in diamond: an application to qualitative all-optical magnetic imaging. *New Journal of Physics*, 14(10):103033, 2012.
- [33] J Teissier, A Barfuss, P Appel, E Neu, and P Maletinsky. Strain coupling of a nitrogen-vacancy center spin to a diamond mechanical oscillator. *Physical review letters*, 113(2):020503, 2014.
- [34] VM Acosta, A Jarmola, E Bauch, and D Budker. Optical properties of the nitrogen-vacancy singlet levels in diamond. *Physical Review B*, 82(20):201202, 2010.
- [35] Lachlan J Rogers, Marcus W Doherty, Michael SJ Barson, Shinobu Onoda, Teraji Ohshima, and Neil B Manson. Singlet levels of the nv- centre in diamond. *New Journal of Physics*, 17(1):013048, 2015.
- [36] LJ Rogers, S Armstrong, MJ Sellars, and NB Manson. Infrared emission of the nv centre in diamond: Zeeman and uniaxial stress studies. *New Journal of Physics*, 10(10):103024, 2008.
- [37] RJ Epstein, FM Mendoza, YK Kato, and DD Awschalom. Anisotropic interactions of a single spin and dark-spin spectroscopy in diamond. *Nature physics*, 1(2):94–98, 2005.
- [38] Martial Piotto, Vladimir Saudek, and Vladimir Sklenář. Gradient-tailored excitation for single-quantum nmr spectroscopy of aqueous solutions. *Journal of biomolecular NMR*, 2(6):661–665, 1992.
- [39] Liam Hall. Phd thesis, University of Melbourne.
- [40] A Jarmola, VM Acosta, K Jensen, S Chemerisov, and D Budker. Temperature-and magnetic-field-dependent longitudinal spin relaxation in nitrogen-vacancy ensembles in diamond. *Physical review letters*, 108(19):197601, 2012.
- [41] Cornelius Kratzer. *Hochauflösende optische Spektroskopie am Pd(dphpy)(CO)-Triplet-Emitter und Untersuchungen zum Energietransfer in einem quasi-zweidimensionalen Tb [Au(CN)₂]₃ · 3 H₂ O-Halbleiter*. Dissertation, Universität Regensburg, 2004.

- [42] Marlan O Scully and M Suhail Zubairy. *Quantum optics*. Cambridge university press, 1997.
- [43] Jeronimo R Maze, Anaïs Dréau, Victor Waselowski, Hector Duarte, Jean-François Roch, and Vincent Jacques. Free induction decay of single spins in diamond. *New Journal of Physics*, 14(10):103041, 2012.
- [44] Nir Bar-Gill, LM Pham, Chinmay Belthangady, David Le Sage, Paola Cappellaro, JR Maze, MD Lukin, Amir Yacoby, and Ronald Walsworth. Suppression of spin-bath dynamics for improved coherence of multi-spin-qubit systems. *Nature communications*, 3:858, 2012.
- [45] C. L. Degen, F. Reinhard, and P. Cappellaro. Quantum sensing. *ArXiv e-prints*, November 2016.
- [46] Y Romach, C Müller, T Unden, LJ Rogers, T Isoda, Kohei M Itoh, M Markham, A Stacey, J Meijer, S Pezzagna, et al. Spectroscopy of surface-induced noise using shallow spins in diamond. *Physical review letters*, 114(1):017601, 2015.
- [47] John David Jackson. *klassische Elektrodynamik*. Walter de Gruyter, 2006.
- [48] Ramamurti Shankar. *Principles of quantum mechanics*. Springer Science & Business Media, 2012.
- [49] Robert H Webb. Confocal optical microscopy. *Reports on Progress in Physics*, 59(3):427, 1996.
- [50] Julia Michl, Tokuyuki Teraji, Sebastian Zaiser, Ingmar Jakobi, Gerald Waldherr, Florian Dolde, Philipp Neumann, Marcus W Doherty, Neil B Manson, Junichi Isoya, et al. Perfect alignment and preferential orientation of nitrogen-vacancy centers during chemical vapor deposition diamond growth on (111) surfaces. *Applied Physics Letters*, 104(10):102407, 2014.
- [51] M Lesik, A Tallaire, J Achard, O Brinza, L William, M Chipaux, L Toraille, T Debuisschert, A Gicquel, JF Roch, et al. Preferential orientation of nv defects in cvd diamond films grown on (113)-oriented substrates. *Diamond and Related Materials*, 56:47–53, 2015.
- [52] Group of Prof. Dr. Jan Meijer. Info slides about 113 oriented sample.
- [53] Johan F Prins. Vacancy diffusion and trapping in electron-irradiated type iaa diamonds. *Diamond and related materials*, 10(1):87–93, 2001.

- [54] Toeno Van der Sar, Francesco Casola, Ronald Walsworth, and Amir Yacoby. Nanometre-scale probing of spin waves using single electron spins. *Nature communications*, 6, 2015.
- [55] Simon M Sze and Kwok K Ng. *Physics of semiconductor devices*. John wiley & sons, 2006.
- [56] JoHoNo Loubser and JoA van Wyk. Electron spin resonance in the study of diamond. *Reports on Progress in Physics*, 41(8):1201, 1978.
- [57] WV Smith, PP Sorokin, IL Gelles, and GJ Lasher. Electron-spin resonance of nitrogen donors in diamond. *Physical Review*, 115(6):1546, 1959.
- [58] Lukas Novotny and Bert Hecht. *Principles of nano-optics*. Cambridge university press, 2012.
- [59] Elke Neu, Patrick Appel, Marc Ganzhorn, Javier Miguel-Sánchez, Margarita Lesik, Vianney Mille, Vincent Jacques, Alexandre Tallaire, Jocelyn Achard, and Patrick Maletinsky. Photonic nano-structures on (111)-oriented diamond. *Applied physics letters*, 104(15):153108, 2014.